Uncertainty quantification in Bayesian operational modal analysis with multiple modes and multiple setups

Zuo Zhu[1], Siu-Kui Au[2]

[1]Corresponding author. Institute for Risk and Uncertainty and School of Engineering, University of Liverpool, United Kingdom. Email: zhuzuo@liverpool.ac.uk
[2] School of Civil and Environmental Engineering, Nanyang Technological University, Singapore. Email: ivanau@ntu.edu.sg

Abstract

In full-scale ambient vibration tests, multiple setups are often performed for measurement when it is demanded to obtain a detailed mode shape with more measured degrees of freedom than the available number of synchronous data channels. In a previous work, a Bayesian operational modal analysis framework for the general case of multiple modes identified with ambient data from multiple setups was developed, together with an Expectation-Maximisation algorithm for efficiently calculating the most probable value (MPV) of modal parameters. Complementing the previous effort, this work investigates the posterior uncertainty of the modal parameters in terms of their posterior covariance matrix. Mathematically, the posterior covariance matrix is equal to the inverse of the Hessian of negative log-likelihood function at the MPV. The computational issues are investigated and analytical expressions for the Hessian matrix are derived, allowing the covariance matrix to be determined efficiently and accurately without resorting to the finite difference method. The proposed algorithm is verified with synthetic data, where the Bayesian and frequentist statistics are compared, and the effect of reference location is investigated. The developed computational tools are also applied to investigate identification uncertainty with field data, where associated practical issues are also discussed.

Keywords

BAYOMA; Uncertainty quantification; Operational modal analysis; Close modes; Multiple setups

1 Introduction

Operational modal analysis (OMA) [1,2] aims at identifying structural modal properties (e.g., natural frequencies, damping ratios and mode shapes) using ‘output-only’ ambient vibration

response data. It has received considerable attention in the dynamic tests of civil structures for its high implementation economy. An increasing number of ambient vibration tests [3–8] have been performed over the last few decades. The identified modal parameters play an important role in many downstream applications, e.g., model updating [9–12], damage detection [13–15] and structural health monitoring [16–19].

In OMA, it is often required to obtain a detailed mode shape with a large number of degrees of freedom (DOFs) but using a limited number of sensors (due to, e.g., limited instrumentation budget or manpower). It is a common practice to plan multiple setups for the measurements. In a multiple-setup setting, some reference sensors are placed at the same location in different setups to allow them to share some common information. In contrast, the remaining sensors are roved progressively to different locations over different setups until all the DOFs of interest are measured. Different kinds of methods exist to analyse the data from multiple setups. Conventionally, modal parameters in each setup are first identified using the corresponding data. The 'global mode shapes' covering all the measured DOFs are then assembled from the 'local mode shapes' in different setups by, e.g., local least squares method or global least squares method [20]. Such a strategy is referred as 'post-identification approach' in some literature [21,22]. This kind of approach requires one to match the identified modes among different setups before the mode shape assembly. The global mode shapes can also be assembled by 'pre-identification approach'. See, e.g., [23–25]. The datasets from multiple setups are first merged to a global one that will be used for modal identification. This kind of approach is convenient for analysis in implementation as the modal identification is only performed once. However, it assumes that all modal parameters are time-invariant in all setups, which could be a major modeling error source.

A Bayesian approach provides a fundamental means to process the data from multiple setups and make the inference on modal parameters in a manner strictly consistent with probability logic and modelling assumptions [26]. A Fast algorithm [27] has been recently developed based on the Fast Fourier Transform (FFT) of OMA data in the previous work, allowing the modal parameters to be determined efficiently in the general case of multiple (possibly close) modes even with a large number of measured DOFs. The modal parameters other than mode shapes need not be the same in different setups, allowing for more robustness in the identification model. Comparison between the Bayesian and some existing methods [26,27] revealed that the Bayesian method tends to be more robust to the data quality, giving physically reasonable mode shapes in the case of low data quality where other methods failed to do so.

Due to the absence of loading information in OMA, the identified modal properties often have significantly higher uncertainty than their counterparts from free or forced vibration tests (known input) where the signal-to-noise (s/n) ratio can be achieved to an adequate level. Quantifying the identification uncertainty is therefore an essential task in OMA. The techniques for uncertainty quantification have been developed from both frequentist and Bayesian perspectives. In a frequentist context, uncertainty refers to the variance of the estimates over hypothetical repeated experiments, often derived based on the first-order sensitivity of the modal parameters to the perturbation of the measured data [28]. The uncertainty in the stochastic subspace identification (SSI) method has been developed for both single-setup [29] and multiple-setup data [30]. In [31], an efficient algorithm has been developed to facilitate the computation of the uncertainty in SSI. Uncertainty quantification algorithm has also been developed for the Eigensystem Realization Algorithm-based algorithm [32]. In a Bayesian context, the modal parameters are modelled as random variables with a probability distribution. The associated uncertainty depends on the datasets rather than the unknown 'true' modal parameters. A Bayesian approach provides a fundamental means to explicitly address the uncertainty, where the posterior distribution of modal parameters can be well approximated by a Gaussian distribution for sufficiently long data [33]. The identification uncertainty is often described by the posterior covariance matrix, which is mathematically equal to the inverse of the Hessian of negative log-likelihood function (NLLF) at the most probable value of modal parameters. The analytical expressions for quantifying the uncertainty have been developed in different settings, e.g., well-separated modes with both single-setup [34] and multiple-setup data [35], close modes with single-setup data [36] and asynchronous data [37]. The connection between Bayesian and frequentist uncertainty is investigated in [38,39].

This work is concerned with Bayesian operational modal analysis in the general context for multiple modes using ambient data from multiple setups. In a previous work [27], the problem has been formulated mathematically and an efficient method based on the Expectation-Maximisation algorithm has been developed to calculate the most probable value of modal parameters (which is akin to the 'best' estimate in non-Bayesian methods). The method was investigated with synthetic data and applied to field data, although the study was limited to the most probable value only. Identification uncertainty was not investigated because efficient computational tools had not yet been developed. Complementing the previous effort, this work investigates the identification uncertainty, where an efficient method for calculating the posterior covariance matrix of modal parameters is developed and investigated with synthetic

and field data. Analytical expressions for the posterior covariance matrix are derived, allowing the uncertainty to be quantified in an accurate and efficient manner without resorting to the finite difference method and brute-force matrix inverse (of Hessian matrix of NLLF, which is numerically ill-conditioned). This work is organised as follows. Bayesian OMA formulation with multiple-setup data is first reviewed in Section 2. Analytical investigations are performed in Section 3. The computational issues are addressed and the expressions of the posterior covariance matrix are derived. In Section 4, the proposed algorithm is verified with synthetic data. It is then applied to field data in Section 5. The paper is concluded in Section 6.

2 Bayesian OMA for multiple setups

In this section, we briefly review the Bayesian OMA (BAYOMA) formulation with multiple-setup data. One may refer to [1] for the general discussion of BAYOMA. Let $\left\{\hat{\ddot{\mathbf{x}}}_j^{(r)}\right\}_{j=0}^{N_r-1}\left(n_r\times 1\right)$ be the measured ambient acceleration data in Setup r (r = 1, …, n_s; n_s is the number of setups) with n_r and N_r respectively being the number of measured DOFs and samples per data channel in this setup. Its (one-sided) scaled FFT at frequency $\mathrm{f}_k^{(r)}=k/\left(N_r\Delta t_r\right)\left(\mathrm{Hz}\right)$ is defined as $\hat{\mathcal{F}}_k^{(r)}=\sqrt{2\Delta t_r/N_r}\sum_{j=0}^{N_r-1}\hat{\ddot{\mathbf{x}}}_j^{(r)}e^{-2\pi\mathbf{i}jk/N_r}$ where Δt_r (sec) is the sampling time interval and $\mathbf{i}^2$ = -1. In BAYOMA, linearly classically damped dynamics is assumed, which is the conventional assumption in structural dynamic analysis and design. Having the same assumption can make the identified results directly transferable. Assuming that there are m dominated modes within the resonance band, referred as Modes 1, 2, …, m, the scaled FFT of the measured data is modelled as $\hat{\mathcal{F}}_k^{(r)}=\boldsymbol{\Phi}_r\ddot{\boldsymbol{\eta}}_k^{(r)}+\boldsymbol{\varepsilon}_k^{(r)}$ where $\boldsymbol{\Phi}_r=\left[\mathbf{v}_{r1},\cdots,\mathbf{v}_{rm}\right]\in R^{n_r\times m}$ whose i-th column v_{ri} is the 'local mode shape' of the i-th mode covering the measured DOFs only in Setup r; $\boldsymbol{\varepsilon}_k^{(r)}\in C^{n_r\times 1}$ denotes the scaled FFT of the prediction error (e.g., data noise and modelling error) assumed to be independent and identically distributed (i.i.d.) among different DOFs with a common power spectral density (PSD) $S_e^{(r)}$ within the band; $\ddot{\boldsymbol{\eta}}_k^{(r)}\in C^{m\times 1}$ is the scaled FFT of modal acceleration response at frequency $\mathrm{f}_k^{(r)}$ whose i-th entry time-domain counterpart satisfies $\ddot{\eta}_i^{(r)}\left(t\right)+2\zeta_i^{(r)}\omega_i^{(r)}\dot{\eta}_i^{(r)}\left(t\right)+\omega_i^{(r)2}\eta_i^{(r)}\left(t\right)=p_i^{(r)}\left(t\right)$ where $\omega_i^{(r)}=2\pi f_i^{(r)}\left(\mathrm{rad/s}\right)$; $f_i^{(r)}$ and $\zeta_i^{(r)}$ are respectively the natural frequency and damping ratio of Mode i in Setup r; $p_i^{(r)}$ is the modal force. In OMA, the modal forces $\left\{p_i^{(r)}\right\}_{i=1}^{m}$ are not measured and assumed to be stochastic

stationary with a constant PSD matrix $\mathbf{S}^{(r)} \in C^{m\times m}$ within the selected band (so only band-limited white).

In a multiple-setup test, different setups are often performed during different time periods and hence possibly under different environmental conditions. The modal parameters other than mode shapes need not be the same among different setups. Let $\boldsymbol{\theta}$ denote the modal parameters to be identified. It comprises $\left\{\left\{f_i^{(r)}\right\}_{i=1}^{m}, \left\{\zeta_i^{(r)}\right\}_{i=1}^{m}, \mathbf{S}^{(r)}, S_e^{(r)}\right\}_{r=1}^{n_s}$ and $\boldsymbol{\Phi} = \left[\boldsymbol{\varphi}_1 \quad \cdots \quad \boldsymbol{\varphi}_m\right]$ where $\boldsymbol{\varphi}_i \in R^{n\times 1}$ is the *i-th* global mode shape covering all the DOFs measured, assumed to be normalised to unity in BAYOMA. To relate the global mode shape to the local one in Setup *r*, a selection matrix $\mathbf{L}_r \in R^{n_r\times n}$ is defined [20], such that $\mathbf{v}_{ri} = \mathbf{L}_r\boldsymbol{\varphi}_i \left(\ i = 1,\cdots,m\right)$**.** The (*j*, *k*)-entry of $\mathbf{L}_r$ is 1 if the *j*-th data channel in Setup *r* measures DOF *k* in $\boldsymbol{\varphi}_i$ and zero otherwise.

Using Bayes' theorem and assuming a uniform prior distribution for $\boldsymbol{\theta}$, the posterior probability density function (PDF) of $\boldsymbol{\theta}$ given data $\mathcal{D} = \left\{\left\{\hat{\mathcal{F}}_k^{(1)}\right\}, \cdots, \left\{\hat{\mathcal{F}}_k^{(n_s)}\right\}\right\}$ is proportional to the likelihood function, i.e., $p\left(\boldsymbol{\theta}|\mathcal{D}\right) \propto p\left(\mathcal{D}|\boldsymbol{\theta}\right)$. The latter is derived based on model assumptions and gives the probability distribution of the possible values of data given $\boldsymbol{\theta}$. Assuming that the scaled FFTs of the data collected in different setups are independent, then $p\left(\mathcal{D}|\boldsymbol{\theta}\right) = \prod_{r=1}^{n_s} p\left(\left\{\hat{\mathcal{F}}_k^{(r)}\right\}|\boldsymbol{\theta}\right)$. In implementation, it is more convenient to work with the negative log-likelihood function (NLLF) for computation and analysis, i.e., $L\left(\boldsymbol{\theta}\right) = -\ln p\left(\mathcal{D}|\boldsymbol{\theta}\right)$, such that $p\left(\boldsymbol{\theta}|\mathcal{D}\right) \propto \exp\left(-L\left(\boldsymbol{\theta}\right)\right)$. It can be shown that [27]:

$$L\left(\boldsymbol{\theta}\right) = -\ln p\left(\mathcal{D}|\boldsymbol{\theta}\right) = \sum_{r=1}^{n_s} L_r \tag{1}$$

where

$$L_r = n_r N_f^{(r)} \ln \pi + \sum_k \ln\left|\mathbf{E}_k^{(r)}\right| + \sum_k \hat{\mathcal{F}}_k^{(r)*} \mathbf{E}_k^{(r)-1} \hat{\mathcal{F}}_k^{(r)} \tag{2}$$

and the sums are over all frequencies in the selected band; $N_f^{(r)}$ is the number of FFT points in the selected band of Setup *r*; $\mathbf{E}_k^{(r)}$ is the theoretical PSD of the data, which is given by

$$\mathbf{E}_k^{(r)} = E\left[\hat{\mathcal{F}}_k^{(r)} \hat{\mathcal{F}}_k^{(r)*} \middle| \boldsymbol{\theta}\right] = \boldsymbol{\Phi}_r \mathbf{H}_k^{(r)} \boldsymbol{\Phi}_r^T + S_e^{(r)} \mathbf{I}_{n_r} \tag{3}$$

where $\mathbf{H}_k^{(r)} = \mathbf{h}_k^{(r)} \mathbf{S}^{(r)} \mathbf{h}_k^{(r)*}$ and '*' denotes the complex conjugate transpose; $\mathbf{h}_k^{(r)} = diag\left(h_{1k}^{(r)}, \cdots, h_{mk}^{(r)}\right)$ is a diagonal matrix with the *i*-th diagonal entry being the frequency response function corresponding to Mode *i* and given by (for acceleration data)

$$h_{ik}^{(r)} = \frac{1}{1 - \beta_{ik}^{(r)2} - 2\zeta_i^{(r)} \beta_{ik}^{(r)} \mathbf{i}} \qquad \beta_{ik}^{(r)} = \frac{f_i^{(r)}}{\mathrm{f}_k^{(r)}} \tag{4}$$

The formulation of BAYOMA has made use of the result that for long data the scaled FFT of a stationary stochastic process asymptotically follows a (circular symmetric) complex Gaussian distribution and they are independent at different frequencies. The method is robust to non-Gaussian excitations because in this case the FFT can still be practically Gaussian by virtue of the Central Limit Theorem; see Section 10.2.1 of [1] for further details. By minimising the NLLF in (1), one can obtain the most probable value (MPV) of modal parameters. However, direct optimisation based on the original formulation is impractical, especially for the case with a large number of DOFs and close modes. A fast algorithm has been proposed, allowing the MPV to be determined efficiently. Details can be found in [27].

3 Posterior uncertainty

Besides MPV, posterior uncertainty is also of concern in OMA. In a Bayesian context, it can be quantified in terms of the posterior covariance matrix of the modal parameters. For typical data length in applications, modal identification is a globally identifiable problem. The posterior PDF has a unique maximum at the MPV $\hat{\boldsymbol{\theta}}$. Equivalently, the NLLF has a unique minimum at the MPV. Without loss of generality, we arrange the set of modal parameters as a one-dimensional vector:

$$\boldsymbol{\theta} = \left[\{ f_i^{(r)}, \zeta_i^{(r)}, S_{ii}^{(r)}, U_{ij}^{(r)}, V_{ij}^{(r)}, S_e^{(r)} : i = 1, \cdots, m;\ j < i; r = 1, \cdots n_s \}; vec\left(\boldsymbol{\Phi}\right) \right] \tag{5}$$

where $S_{ii}^{(r)}$ is the diagonal entry of $\mathbf{S}^{(r)}$; $U_{ij}^{(r)}$ and $V_{ij}^{(r)}$ denote the real and imaginary part of $S_{ij}^{(r)}$ (i.e., the (*i*, *j*)-entry of $\mathbf{S}^{(r)}$), respectively; $vec\left(\boldsymbol{\Phi}\right) = \left[\boldsymbol{\varphi}_1; \cdots; \boldsymbol{\varphi}_m\right] \in R^{nm \times 1}$. The total number of (real-valued) parameters in $\boldsymbol{\theta}$ is $n_{\boldsymbol{\theta}} = n_s \left(m+1\right)^2 + nm$. It can be shown that the posterior PDF $p\left(\boldsymbol{\theta} | \mathcal{D}\right)$ can be approximated by a Gaussian PDF [33]. The posterior covariance matrix of the modal parameters given data is equal to the inverse of the Hessian of the NLLF at the MPV. Note that the mode shapes are subjected to norm constraints, which must be accounted for in

the evaluation of the Hessian matrix. In [40], a theoretical framework was developed to evaluate the Hessian matrix of a function under constraints in a systematic manner, which will be used to handle the mode shape constraints in this work.

3.1 Norm constraints on mode shapes

In this section, we handle the norm constraints on mode shapes based on the theory developed in [40]. Let $\{G_i(\boldsymbol{\theta})\}_{i=1}^{m}$ be the norm constraint equations on mode shapes, i.e.,

$$G_i(\boldsymbol{\theta}) = 1 - \boldsymbol{\varphi}_i^T \boldsymbol{\varphi}_i \tag{6}$$

Define a set of free parameters $\mathbf{u}$ and a function $\boldsymbol{\theta} = \mathrm{v_c}(\mathbf{u})$ that maps $\mathbf{u}$ to $\boldsymbol{\theta}$ by

$$\mathbf{u} = \begin{bmatrix} \varpi \\ \boldsymbol{\varphi}_1 \\ \vdots \\ \boldsymbol{\varphi}_m \end{bmatrix} \qquad \mathbf{v}_c(\mathbf{u}) = \begin{bmatrix} \varpi \\ \|\boldsymbol{\varphi}_1\|^{-1} \boldsymbol{\varphi}_1 \\ \vdots \\ \|\boldsymbol{\varphi}_m\|^{-1} \boldsymbol{\varphi}_m \end{bmatrix} \tag{7}$$

where ϖ comprises the real-valued modal parameters other than mode shapes. With the definition in (7), the constraints on mode shapes are always satisfied, i.e., $G_i(\mathbf{v}_c(\mathbf{u})) \equiv 0 \, (i = 1, \cdots, m)$ for any $\mathbf{u}$. The NLLF in (1) can then be formulated w.r.t. $\mathbf{u}$ by the composite function $L_c(\mathbf{u}) = L(\mathbf{v}_c(\mathbf{u}))$. In [40], it is shown that the posterior covariance matrix of the set of modal parameters $\boldsymbol{\theta}$ is given by

$$\hat{\mathbf{C}} = (\nabla \hat{\mathbf{v}}_c) \hat{\mathbf{C}}_{\mathbf{u}} (\nabla \hat{\mathbf{v}}_c)^T \tag{8}$$

where the hat '^' on the quantity denotes that it is evaluated at the MPV; $\nabla \hat{\mathbf{v}}_c \in R^{n_{\boldsymbol{\theta}} \times n_{\boldsymbol{\theta}}}$ denotes the gradient of $\mathrm{v_c}(\mathbf{u})$; $\hat{\mathbf{C}}_{\mathbf{u}}$ is the posterior covariance matrix of the set of free parameters $\mathbf{u}$, equal to the inverse of $\nabla^2 \hat{L}_c$ (Hessian of L_c w.r.t. $\mathbf{u}$ at the MPV). Note that $\nabla^2 \hat{L}_c$ has m zero eigenvalues with eigenvectors along the mode shape directions and is therefore not invertible because L_c is invariant to the scaling of the mode shapes $\boldsymbol{\varphi}_i$. Nevertheless, this singularity is immaterial to the posterior uncertainty of $\boldsymbol{\theta}$ because the mode shape uncertainty is orthogonal to the direction of the MPV of $\hat{\boldsymbol{\varphi}}_i$. Consequently, the inverse of $\nabla^2 \hat{L}_c$ (hence $\hat{\mathbf{C}}_{\mathbf{u}}$) can be evaluated via its eigen-basis representation ignoring the first m zero eigenvalues arising from constraint singularity, i.e.,

$$\hat{\mathbf{C}}_{\mathbf{u}} = \sum_{i=m+1}^{n_\theta} \lambda_i^{-1} \mathbf{w}_i \mathbf{w}_i^T \tag{9}$$

where $\{\lambda_i\}_{i=m+1}^{n_\theta}$ are the non-zero eigenvalues of $\nabla^2 \hat{L}_c$ at the MPV with the corresponding eigenvectors $\{\mathbf{w}_i\}_{i=m+1}^{n_\theta}$.

It is generally more complicated to derive $\nabla^2 \hat{L}_c$ compared to the Hessian of L w.r.t $\boldsymbol{\theta}$ because $L_c(\mathbf{u})$ is a composite function of $\mathbf{u}$. Based on Lagrange multiplier concepts, $\nabla^2 \hat{L}_c$ can be calculated in terms of the gradients and Hessian of $L(\boldsymbol{\theta})$, $G(\boldsymbol{\theta})$ and $\mathbf{v}_c(\mathbf{u})$ [40]:

$$\nabla^2 \hat{L}_c = (\nabla \hat{\mathbf{v}}_c)^T \left(\nabla^2 \hat{L} + \sum_{i=1}^{m} \hat{\lambda}_i \nabla^2 \hat{G}_i \right) (\nabla \hat{\mathbf{v}}_c) \tag{10}$$

where $\nabla^2 \hat{L}$ is the Hessian of the NLLF in (1) w.r.t. $\boldsymbol{\theta}$ **(**ignoring the mode shape constraints) and

$$\boldsymbol{\lambda} = \begin{bmatrix} \hat{\lambda}_1 \\ \vdots \\ \hat{\lambda}_m \end{bmatrix} = -\left[(\nabla \hat{\mathbf{G}})(\nabla \hat{\mathbf{G}})^T \right]^{-1} (\nabla \hat{\mathbf{G}})(\nabla \hat{L})^T \tag{11}$$

$$\nabla \hat{L} = \nabla L(\boldsymbol{\theta})\big|_{\boldsymbol{\theta}=\hat{\boldsymbol{\theta}}} \in R^{1\times n_\theta} \quad \nabla^2 \hat{L} = \nabla^2 L(\boldsymbol{\theta})\big|_{\boldsymbol{\theta}=\hat{\boldsymbol{\theta}}} \in R^{n_\theta \times n_\theta} \quad \nabla \hat{\mathbf{G}} = \begin{bmatrix} \nabla \hat{G}_1 \\ \vdots \\ \nabla \hat{G}_m \end{bmatrix} \in R^{m\times n_\theta} \tag{12}$$

$$\nabla \hat{\mathbf{v}}_c = \nabla \mathbf{v}_c(\mathbf{u})\big|_{\mathbf{u}=\hat{\mathbf{u}}} \in R^{n_\theta \times n_\theta} \quad \nabla \hat{G}_i = \nabla G_i(\boldsymbol{\theta})\big|_{\boldsymbol{\theta}=\hat{\boldsymbol{\theta}}} \in R^{1\times n_\theta} \quad \nabla^2 \hat{G}_i = \nabla^2 G_i(\boldsymbol{\theta})\big|_{\boldsymbol{\theta}=\hat{\boldsymbol{\theta}}} \in R^{n_\theta \times n_\theta} \tag{13}$$

Based on (6), the derivatives of $G(\boldsymbol{\theta})$ are given by

$$\nabla_{\varpi} \hat{G}_i = \mathbf{0} \quad \nabla^2_{\varpi} \hat{G}_i = \mathbf{0} \quad \nabla_{\boldsymbol{\varphi}_j} \hat{G}_i = -2\hat{\boldsymbol{\varphi}}_i^T \delta_{ij} \quad \nabla^2_{\boldsymbol{\varphi}_j} \hat{G}_i = -2\mathbf{I}_n \delta_{ij} \tag{14}$$

where δ_{ij} is the Kronecker Delta (1 if $i = j$, zero otherwise). Substituting (14) into (11) and rearranging gives

$$\hat{\lambda}_i = \frac{1}{2} (\nabla_{\boldsymbol{\varphi}_i} L) \boldsymbol{\varphi}_i \tag{15}$$

Using (14), we can also obtain

$$\sum_{i=1}^{m} \hat{\lambda}_i \nabla^2 \hat{G}_i = \begin{bmatrix} \mathbf{0}_{n_\varpi \times n_\varpi} & & & \\ & -2\hat{\lambda}_1 \mathbf{I}_n & & \\ & & \ddots & \\ & & & -2\hat{\lambda}_m \mathbf{I}_n \end{bmatrix} \tag{16}$$

where $n_\varpi = n_s \left(m+1\right)^2$ is the total number of (real-valued) parameters in ϖ. By noting that $\nabla_{\boldsymbol{\varphi}_i} \left(\left\| \boldsymbol{\varphi}_i \right\|^{-1} \boldsymbol{\varphi}_i \right) = \mathbf{I}_n - \boldsymbol{\varphi}_i \boldsymbol{\varphi}_i^T$ for $\left\| \boldsymbol{\varphi}_i \right\| = 1$,

$$\nabla \hat{\mathbf{v}}_c = \begin{bmatrix} \mathbf{I}_{n_\varpi \times n_\varpi} & & & \\ & \mathbf{I}_n - \boldsymbol{\varphi}_1 \boldsymbol{\varphi}_1^T & & \\ & & \ddots & \\ & & & \mathbf{I}_n - \boldsymbol{\varphi}_m \boldsymbol{\varphi}_m^T \end{bmatrix} \tag{17}$$

In (10), it remains to determine $\nabla \hat{L}$ and $\nabla^2 \hat{L}$, whose analytical expressions will be derived in the next section.

3.2 Derivatives of NLLF

The analytical derivatives of $L(\boldsymbol{\theta})$ w.r.t. $\boldsymbol{\theta}$ (ignoring the norm constraints on mode shapes) are investigated in this section. Direct differentiation based on the original formulation in (1) involves the matrix computation of dimension n_r, which increases drastically with the number of measured DOFs. In view of this, a condensed form of NLLF is employed in this work for computing the derivatives:

$$L\left(\boldsymbol{\theta}\right) = L_e + L_J + L_H + L_Q \tag{18}$$

with

$$L_e = \ln \pi \sum_{r=1}^{n_s} n_r N_f^{(r)} + \sum_{r=1}^{n_s} \left(n_r - m\right) N_f^{(r)} \ln S_e^{(r)} \tag{19}$$

$$L_J = \sum_{r=1}^{n_s} \sum_{k} \ln \left| \mathbf{J}_k^{(r)} \right| \quad L_H = \sum_{r=1}^{n_s} \sum_{k} \ln \left| \mathbf{H}_k^{(r)} \right| \tag{20}$$

$$L_Q = \sum_{r=1}^{n_s} S_e^{(r)-1} \left(d^{(r)} - Q^{(r)} \right) \qquad Q^{(r)} = \sum_{k} \mathbf{s}_k^{(r)*} \mathbf{J}_k^{(r)-1} \mathbf{s}_k^{(r)} \tag{21}$$

where $d^{(r)} = \sum_k \mathcal{F}_k^{(r)*} \mathcal{F}_k^{(r)}$, $\mathbf{s}_k^{(r)} = \boldsymbol{\Phi}^T \mathbf{L}_r^T \mathcal{F}_k^{(r)}$ and

$$\mathbf{J}_k^{(r)} = S_e^{(r)} \left(\mathbf{H}_k^{(r)} \right)^{-1} + \boldsymbol{\Phi}^T \mathbf{L}_r^T \mathbf{L}_r \boldsymbol{\Phi} \tag{22}$$

To facilitate the presentation of the derivatives, (18) has been divided into four terms. It is derived from (1) by using the identities [41]:

$$\begin{aligned}\left(\mathbf{A}+\mathbf{UCV}\right)^{-1} &= \mathbf{A}^{-1}-\mathbf{A}^{-1}\mathbf{U}\left(\mathbf{C}^{-1}+\mathbf{VA}^{-1}\mathbf{U}\right)^{-1}\mathbf{VA}^{-1}\\ \left|\mathbf{A}+\mathbf{UCV}\right| &= \left|\mathbf{A}\right|\left|\mathbf{C}\right|\left|\mathbf{C}^{-1}+\mathbf{VA}^{-1}\mathbf{U}\right|\end{aligned} \tag{23}$$

for any matrices **A**, **C**, **U**, **V** of appropriate size with **A** and **C** invertible. Details can be found in Appendix A of [27]. By writing the NLLF in this form, the matrices involved in the computation have a dimension of *m*, which is generally much smaller than n_r in implementation.

To facilitate the presentation of the derivatives, they are separated into three parts, namely, the derivatives w.r.t. ϖ (i.e., the modal parameters other than mode shape), the cross derivatives w.r.t. ϖ and $vec(\mathbf{\Phi})$, and the derivatives w.r.t. $vec(\mathbf{\Phi})$. In a multiple-setup test, modal parameters other than mode shapes could vary from one setup to another. The total number of parameters in ϖ is equal to $n_s\left(m+1\right)^2$. Mathematically, the NLLF with multiple setup data (i.e., (1)) is equal to the summation of the NLLF with single setup data except that the mode shapes are now replaced by the local ones confined to the measured DOFs in the corresponding setup. As a result, the derivation of the derivatives w.r.t. ϖ is similar to the case of the single-setup problem in Section 13.7.2 of [1], although it is presented for the present case of multiple setup data for completeness. Details can be found in Appendix A.

The evaluation of the derivatives w.r.t. the mode shapes, however, is computationally challenging as the number of variables in $vec(\mathbf{\Phi})$ ($nm \times 1$) increases drastically with the total number of measured DOFs, which could be quite large in a multiple-setup test. Direct computation w.r.t. each variable in $vec(\mathbf{\Phi})$ is apparently inefficient and also inconvenient for computer-coding. As derived in Appendix B, the gradient of *L* w.r.t. $vec(\mathbf{\Phi})$ can be expressed in a compact form:

$$\frac{\partial L}{\partial vec\left(\mathbf{\Phi}\right)^T} = \mathbf{U}_1+\mathbf{U}_2+\mathbf{U}_3 \tag{24}$$

where

$$\mathbf{U}_1 = 2\sum_{r=1}^{n_s}\sum_k \mathrm{Re}\left[vec\left(\mathbf{A}_r\mathbf{\Phi}\mathbf{J}_k^{(r)-1}\right)^T\right] \qquad \mathbf{U}_2 = 2\sum_{r=1}^{n_s}\sum_k \mathrm{Re}\left[vec\left(-S_e^{(r)-1}\mathbf{D}_k^{(r)}\mathbf{\Phi}\mathbf{J}_k^{(r)-1}\right)^T\right] \tag{25}$$

and

$$\mathbf{U}_3 = 2\sum_{r=1}^{n_s}\sum_{k}\mathrm{Re}\left[vec\left(S_e^{(r)-1}\mathbf{A}_r\boldsymbol{\Phi}\mathbf{J}_k^{(r)-1}\boldsymbol{\Phi}^T\mathbf{D}_k^{(r)}\boldsymbol{\Phi}\mathbf{J}_k^{(r)-1}\right)^T\right] \tag{26}$$

where Re[•] denotes the real part of the subject quantity; $\mathbf{A}_r = \mathbf{L}_r^T\mathbf{L}_r$ and $\mathbf{D}_k^{(r)} = \mathbf{L}_r^T\mathcal{F}_k^{(r)}\mathcal{F}_k^{(r)*}\mathbf{L}_r$. Taking the derivatives of $\partial L/\partial vec(\boldsymbol{\Phi})^T$ in (24) w.r.t. $\boldsymbol{\varpi}$ then gives the cross derivatives of $L(\boldsymbol{\theta})$ w.r.t. $vec(\boldsymbol{\Phi})$ and $\boldsymbol{\varpi}$. The details of the derivation can be found in Appendix C.

As derived in Appendix D, the second derivatives of NLLF w.r.t. $vec(\boldsymbol{\Phi})$ is given by

$$\nabla^2_{vec(\boldsymbol{\Phi})}L = 2\sum_{r=1}^{n_s}\sum_{k}\mathrm{Re}\left[\mathbf{H}_{\boldsymbol{\Phi}1} + \mathbf{H}_{\boldsymbol{\Phi}2} + \frac{\partial vec\left(\boldsymbol{\Phi}^T\right)^T}{\partial vec\left(\boldsymbol{\Phi}\right)}\mathbf{H}_{\boldsymbol{\Phi}3}\right] \tag{27}$$

where

$$\mathbf{H}_{\boldsymbol{\Phi}1} = \mathbf{J}_k^{(r)-1}\otimes\left[\mathbf{L}_r^T\left(\mathbf{I}_{n_r} - \mathbf{C}_k^{(r)T}\right)\mathbf{R}_{1k}^{(r)-T}\mathbf{L}_r\right] \tag{28}$$

$$\mathbf{H}_{\boldsymbol{\Phi}2} = \mathbf{B}_k^{(r)*}\mathcal{F}_k^{(r)}\mathcal{F}_k^{(r)*}\mathbf{B}_k^{(r)}\otimes\left(\mathbf{L}_r^T\mathbf{E}_k^{(r)-T}\mathbf{L}_r\right) \tag{29}$$

$$\mathbf{H}_{\boldsymbol{\Phi}3} = \mathbf{L}_r^T\mathbf{C}_k^{(r)*}\mathbf{B}_k^{(r)}\otimes\left(\mathbf{B}_k^{(r)T}\mathbf{L}_r\right) - \left(\mathbf{L}_r^T\mathbf{B}_k^{(r)}\right)\otimes\left[\mathbf{B}_k^{(r)T}\left(\mathbf{I}_{n_r} - \mathbf{R}_{2k}^{(r)T}\mathbf{R}_{1k}^{(r)-T}\right)\mathbf{L}_r\right] \tag{30}$$

where the superscripted symbol '$-T$' denotes the transpose of the inverse of the matrix; '$\otimes$' denotes Kronecker product; $\mathbf{B}_k^{(r)} = \boldsymbol{\Phi}_r\mathbf{J}_k^{(r)-1} \in C^{n_r\times m}$; $\mathbf{C}_k^{(r)} = \mathcal{F}_k^{(r)}\mathcal{F}_k^{(r)*}\mathbf{E}_k^{(r)-1} \in C^{n_r\times n_r}$; $\mathbf{R}_{1k}^{(r)} = S_e^{(r)-1}\mathbf{E}_k^{(r)} \in C^{n_r\times n_r}$ is the ratio of the theoretical data PSD matrix $\mathbf{E}_k^{(r)}$ to prediction error PSD, reflecting the data s/n ratio in Setup r; $\mathbf{R}_{2k}^{(r)} = S_e^{(r)-1}\mathcal{F}_k^{(r)}\mathcal{F}_k^{(r)*} \in C^{n_r\times n_r}$ also reflects data s/n ratio but now w.r.t. sample PSD of the data. Note that $\mathbf{R}_{1k}^{(r)}$ is generally not equal to $\mathbf{R}_{2k}^{(r)}$ due to the existence of the statistical and modelling error. It is seen that the derivatives w.r.t $vec(\boldsymbol{\Phi})$ can be computed in a compact manner instead of looping through the variables in $vec(\boldsymbol{\Phi})$, hence significantly accelerating the computation especially when the number of measured DOFs n is large.

3.3 Singularity from mode shape constraints

Based on the analysis in Section 3.2, one can assemble the Hessian matrix of NLLF w.r.t. $\boldsymbol{\theta}$ (ignoring the constraints on mode shapes), then the Hessian matrix $\nabla^2\hat{L}_c$ w.r.t. the free

parameters **u** can be obtained using (10). As mentioned before, since L_c is invariant to the scaling of the mode shapes, $\nabla^2\hat{L}_c$ has *m* zero eigenvalues along the mode shape directions and hence cannot be inverted directly. The pseudo-inverse of $\nabla^2\hat{L}_c$ is evaluated using (9) via the eigenvector representation, ignoring the zero eigenvalue components which are associated with constraint singularity. In digital computation, the eigenvalues that are theoretically zero need not be exactly so due to the round-off error. One primitive way is to take the *m* smallest eigenvalues of $\nabla^2\hat{L}_c$ as the ones to be ignored. However, as recently discovered in the uncertainty laws of close modes [42], there could be some eigenvalues that are theoretically small and even smaller than round-off error, e.g., those associated with the uncertainty perpendicular to the mode shape subspace. In such case, it may not be correct to identify the *m* smallest eigenvalues as corresponding to the mode shape singularities to ignore. Note that the eigenvectors theoretically corresponding to the zero eigenvalues should lie in the mode shape subspace but need not be along a particular mode shape direction because any linear combination of the null vectors is still a null vector. In view of this, a more fundamental and robust way to identify these eigenvectors (null vectors) is to look for the first *m* eigenvectors with the largest values of the sum of squares of modal assurance criteria (MAC) with the theoretical null vectors along the mode shape directions. The latter can be expressed as $\sum_{i=1}^{m}\left(\mathbf{v}_i^T\mathbf{w}_j\right)^2$ where $\mathbf{v}_i$ is the null vector along the *i*-th mode shape direction and $\mathbf{w}_j$ ($j = 1, \ldots, n_{\boldsymbol{\theta}}$) is the eigenvector of $\nabla^2\hat{L}_c$.

3.4 Overall procedure

Given the data, the MPV of modal parameters can be identified using the algorithm in [27]. Based on the analysis before, the posterior identification uncertainty can be obtained as follow:

1) Calculate the entries of gradient and Hessian matrix of the NLLF (ignoring the norm constraints on mode shapes) with the help of the derivation in Section 3.2.

2) Calculate the Hessian matrix of the NLLF $\nabla^2\hat{L}_c$ (w.r.t. the free parameters **u**) using (10) with the help of (11)-(17).

3) Perform eigenvector decomposition of $\nabla^2\hat{L}_c$ and calculate its pseudo-inverse using (9) by excluding the first *m* eigenvectors with the largest sum of squares of MAC with the mode shape directions.

4) Calculate the posterior covariance matrix of modal parameters using (8).

5) The posterior coefficient of variation (c.o.v.) of modal parameters other than mode shapes can be evaluated as the ratio of the posterior standard deviation to the MPV. The former is equal to the square root of the corresponding diagonal entry of the posterior covariance matrix.

6) The posterior c.o.v. of the global mode shape can be evaluated as the square root sum of the eigenvalues of the mode shape covariance matrix, which is equal to the corresponding partition of the mode shape in the full covariance matrix [33].

4 Verification with synthetic data

4.1 Shear building

Consider the horizontal vibration of a five-storied shear building with the floor plan measuring 22 m × 22 m, as shown in Fig. 1(a). The height of all stories is 4 m. Assuming rigid floor, the interstory stiffness and mass are summarised in Table 1. The natural frequencies of the first three modes are calculated to be 2.738 Hz, 2.779 Hz and 3.763 Hz, corresponding to the fundamental translational modes along *x*- and *y*- directions, and the fundamental rotational mode. Classical damping is assumed for all modes, with a damping ratio of 1%. This structure is specially designed so that the mode shape values of the second translational and torsional modes are close to zero at Level 4. The structure is subjected to independent and identically distributed (i.i.d.) Gaussian excitations at all the floor levels, with a one-sided root PSD of $0.5\,\mathrm{N}/\sqrt{\mathrm{Hz}}$, $0.5\,\mathrm{N}/\sqrt{\mathrm{Hz}}$ and $3\,\mathrm{N}\cdot\mathrm{m}/\sqrt{\mathrm{Hz}}$ along *x*-, *y*- and rotational directions, respectively. The structural response is calculated using the Newmark scheme. The acceleration response is then assumed to be contaminated by i.i.d. Gaussian white noise at different channels with a one-sided PSD of $S_e = 1(\mu\mathrm{g})^2/\mathrm{Hz}$. The noise is generated by $\mathbf{e}_j = \sqrt{S_e/2\Delta t_r}\,\mathbf{Z}_j$ at time instant $t_j = j\Delta t_r$ $(j = 1,2,\cdots,N)$ where N and $\mathbf{Z}_j$ are respectively the number of samples per data channel and i.i.d. standard Gaussian vector sequence. The test plan is to measure the horizontal vibration at the four corners of all the floors, as indicated by the dots in Fig. 1(a). The total number of measured DOFs is 20 × 2 = 40. It is assumed that only five biaxial sensors are available during the test, requiring five setups to cover all the DOFs of interest. One reference sensor is put at Location 15 on the top floor. The other four sensors move from the first floor to the top floor, as shown in Fig. 1(b). Acceleration data at each setup lasts for 10 minutes at a sampling rate of 50 Hz.

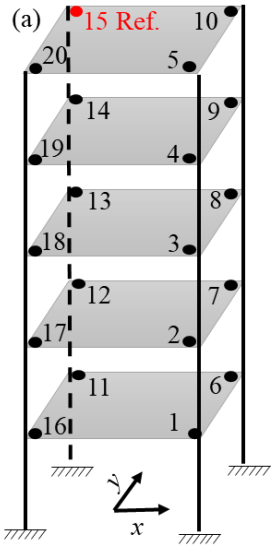

(b)

Setup No.	Floor No.	Roving direction
5	5/F	
4	4/F	
3	3/F	
2	2/F	
1	1/F	

Fig. 1 (a) Shear building with measured DOFs numbered and indicated by dots; (b) measurement plan

Table 1 Properties of shear building

Story	Stiffness			Mass		
	x (kN/mm)	*y* (kN/mm)	Rotation (GN m/rad)	*x* (tonne)	*y* (tonne)	Rotation (ktonne m^2)
1	1000	1030	302	250	250	40
2	1000	1030	302	250	250	40
3	1000	1030	302	250	250	40
4	600	618	181	250	250	40
5	600	618	181	250	250	40

Fig. 2 shows the singular value spectrum calculated using the averaged PSD of the data in Setup 5, where the number of lines significantly above the remaining ones in a resonance band indicates the number of modes. Note that the averaging concept used here is merely for producing a smooth spectrum for better visualisation. We focus on the first six modes, which are labelled with their modal nature in the figure. The prefix 'TX', 'TY' and 'R' represent the translational modes along *x*- and *y*-directions, and rotational mode, respectively. The horizontal bar indicates the selected band whose FFT data will be used for modal identification. The circle indicates the initial guess of natural frequency. Modes TX1 and TY1 are quite close due to the similar interstory stiffness. This is also the case for Modes TX2 and TY2.

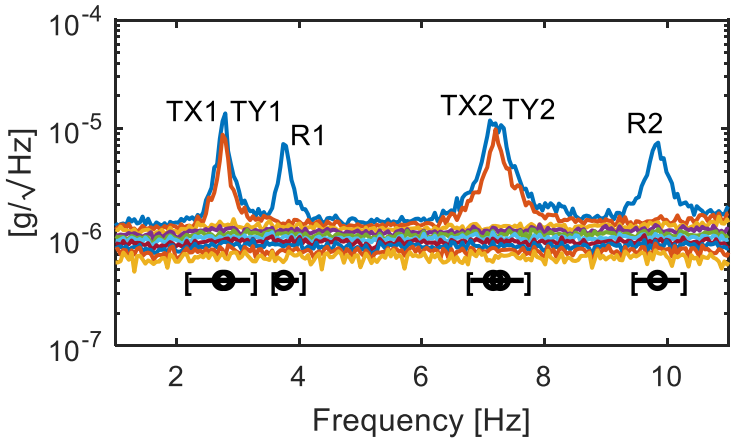

Fig. 2 Singular value spectrum, Setup 5, shear building

4.2 Modal identification

The modal parameters of the structure are identified using the Bayesian multiple-setup algorithm in [27] and their uncertainties are quantified based on the algorithm developed in this work. The MPVs of the modal parameters among different setups are close to each other and they are also close to their exact values (details omitted here). Fig. 3 shows the posterior c.o.v. of natural frequencies and damping ratios for different modes. Different colours indicate the results in different setups. It is seen that the posterior c.o.v. of modal parameters varies from one setup to another. The posterior c.o.v. of natural frequencies (around 0.1%) are much smaller than those of damping ratios (around 10%), which is consistent with common observations. The uncertainties of Modes TX2, TY2 and R2 are smaller than their counterparts of Modes TX1, TY1 and R1. This can be explained by 'uncertainty laws' [43,44], which reveal the relationship between posterior uncertainty and test configuration. It shows that the posterior uncertainty depends on the effective amount of data, which is proportional to the number of cycles of the mode (= natural frequency × data length) in the data. For the same data length, the higher mode tends to be associated with smaller c.o.v. (hence more accurate) since the data contains more cycles of modal oscillation.

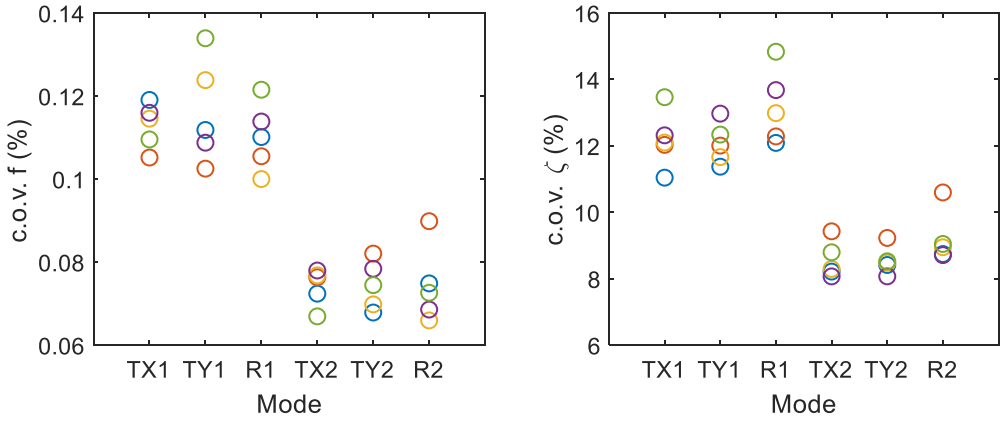

Fig. 3 Posterior c.o.v. of natural frequencies and damping ratios in different setups and different modes

Fig. 4 shows the identified mode shapes where the red and black lines represent the undeformed and deformed shapes, respectively. The natural frequencies and damping ratios are also reported in the figure in terms of the sample mean among the setups. It is seen that the mode shape values at Level 4 are quite small for TX2, TY2 and R2, suggesting that the measured data at this floor may have a relatively lower s/n ratio for these modes. The second row of Table 2 shows the MAC between the identified and exact mode shapes. The values in this row are very close to 1, suggesting that the identified mode shapes are close to the exact ones. Note that these values cannot be calculated in real applications because the exact mode shape is never known. The third row in Table 2 shows the posterior mode shape c.o.v., which can be viewed as the standard deviation of the hyper angle (in radian) between the uncertain and most probable mode shapes (see Section 11.3 in [1]). The last row gives the expected MAC between the posterior uncertain mode shape and its MPV. It is defined as $\rho_i = \left(1+\delta_{\varphi_i}^2\right)^{-1/2}$ where δ_{φ_i} is the mode shape c.o.v. of the *i*-th mode [33]. The expected MAC is defined in a manner analogous to the MAC in the deterministic case and can be used as a global measure for assessing the mode shape quality; the higher, the better. The values of the expected MAC are all close to 1 and consistent with the MAC values.

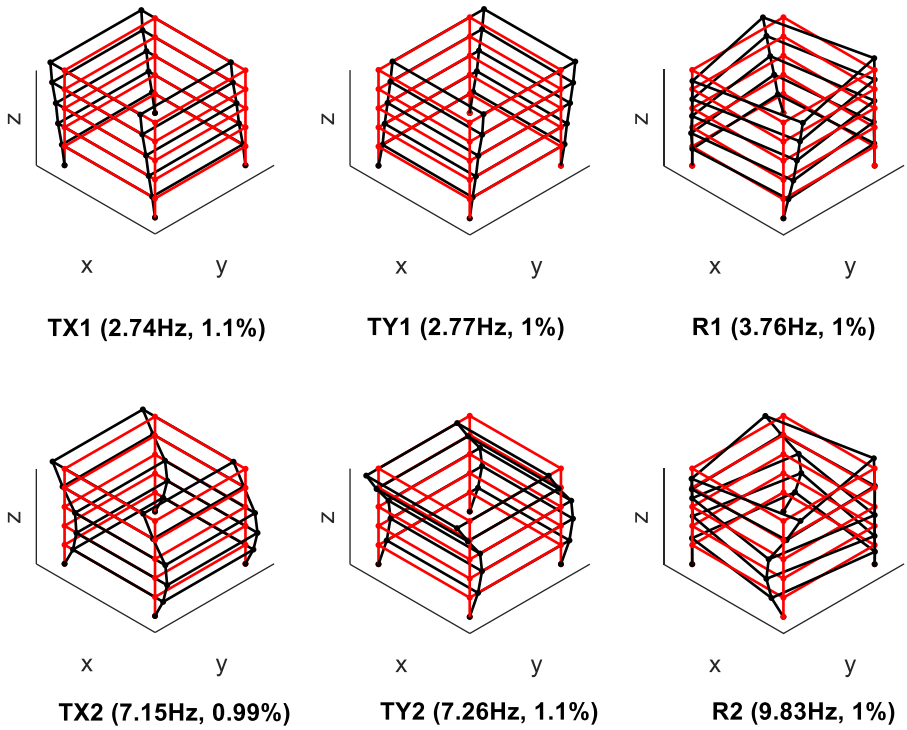

Fig. 4 Identified mode shapes; shear building; values in parenthesis indicate the sample mean of MPVs of natural frequencies and damping ratios among all setups

Table 2 MAC between the identified and exact mode shape, and mode shape c.o.v.

Mode	TX1	TY1	R1	TX2	TY2	R2
MAC	0.9994	0.9992	0.9982	0.9995	0.9997	0.9993
c.o.v. (%)	5.19	5.20	5.38	3.29	3.36	3.57
Expected MAC	0.9987	0.9987	0.9986	0.9995	0.9994	0.9994

4.3 Bayesian versus frequentist statistics

In a Bayesian context, the posterior c.o.v. reflects the remaining uncertainty of modal parameters in the presence of the information from the given data. On the other hand, the identification uncertainty can also be approached from a classical frequentist perspective in terms of the ensemble variance of estimates over statistically identical experiment trials. In this section, the proposed algorithm is verified from a statistical sense. For this purpose, 1000 i.i.d. multiple-setup data sets (10 minutes each) are generated. Accordingly, 1000 results can be obtained in terms of MPV and posterior c.o.v.. Fig. 5 shows the histogram of the MPVs of the identified natural frequencies in Setup 1. It is seen that the shaded bars can be well-fitted by a

Gaussian distribution (red line) with the mean value close to the exact value (dashed black line). This is also the case for damping ratios, as shown in Fig. 6.

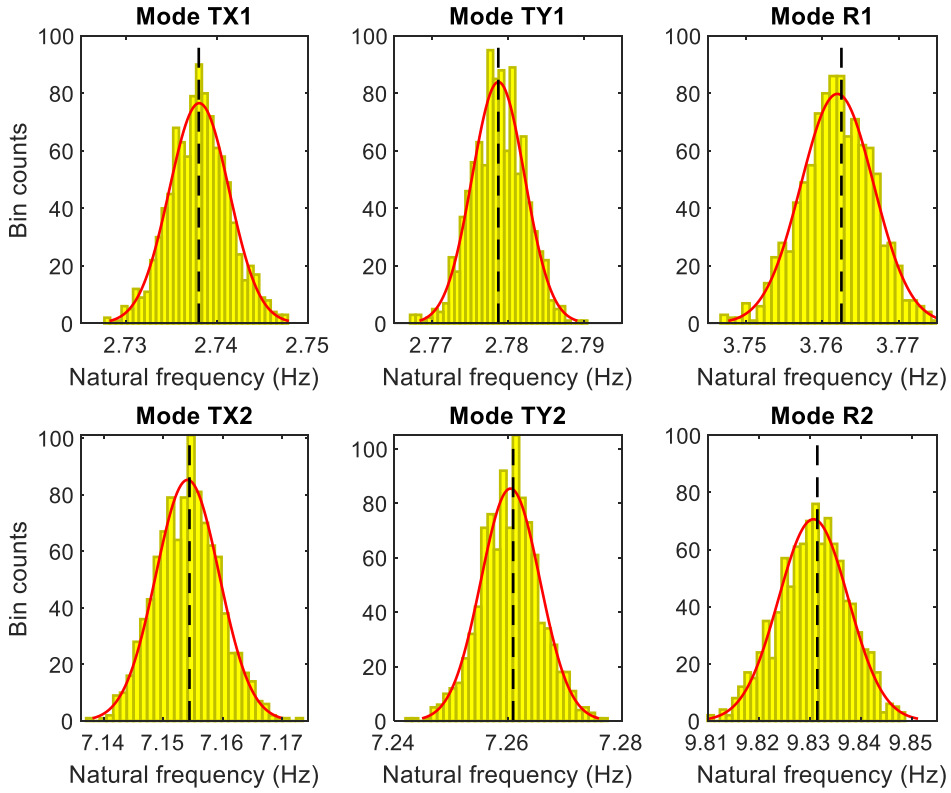

Fig. 5 Histogram of natural frequencies among 1000 trials (shaded bar); red line: fitted Gaussian distribution of histogram; dashed black line: exact value. Shear building

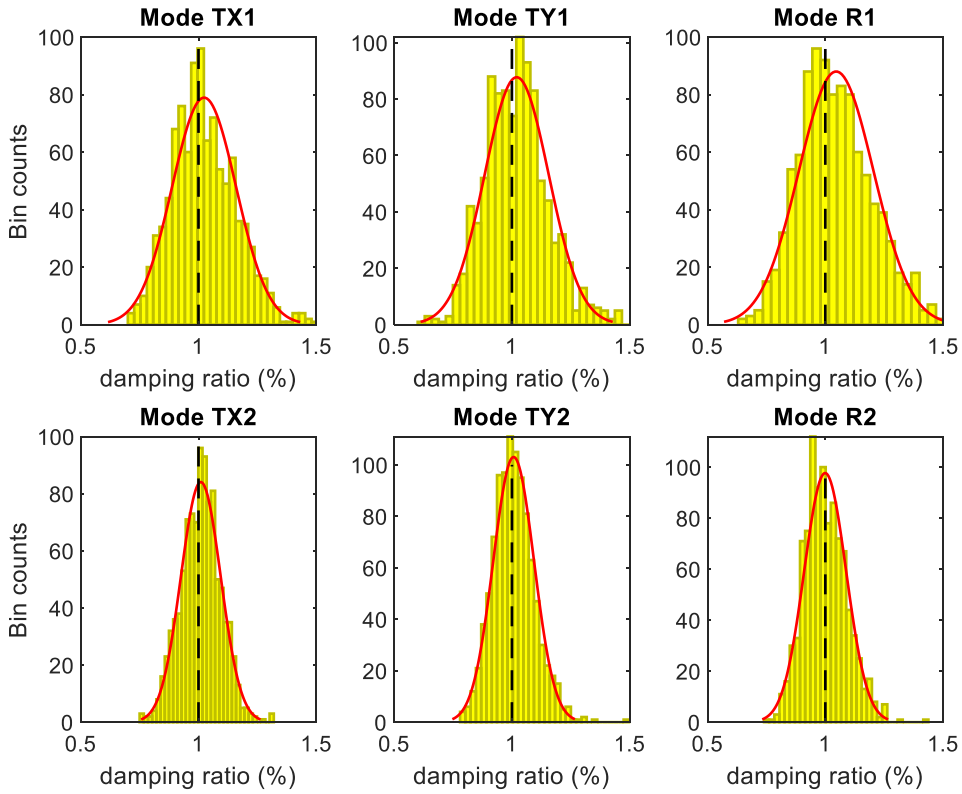

Fig. 6 Histogram of damping ratios among 1000 trials (shaded bar); red line: fitted distribution of histogram; dashed black line: exact value. Shear building

Fig. 7(a) and (b) compare the Bayesian and frequentist statistics of the identified natural frequencies and damping ratios, respectively. The x-axis with the label of 'Freq.' (short for frequentist) shows the sample c.o.v. of the MPVs among the 1000 trials, which is defined as the ratio of sample standard deviation to the sample mean of the MPV. The y-axis with the label of 'Bay.' (short for Bayesian) shows the sample root mean square (RMS) value of the posterior standard deviation divided by the sample mean of the MPV. The circles scatter along the 1:1 (dashed) line, indicating that the posterior c.o.v.s in a Bayesian manner are consistent with their frequentist counterpart. Fig. 7(c) compares the sample and Bayesian statistics of the identified mode shapes. The x-axis shows the sample RMS value of the hyper angles between the identified and exact mode shapes among the 1000 trials while the y-axis shows the RMS value of the posterior mode shape c.o.v.. It is seen that they are also consistent. It should be noted, however, that this is only true when there is no modelling error [39], as in this example with synthetic data. The posterior MPV in a Bayesian context is mathematically equal to the maximum likelihood estimator in classical statistics. For long data and assuming no modelling error, its variance reaches the tightest Cramer Rao Bound value, which coincides with the leading order of the posterior variance in the Bayesian method [39].

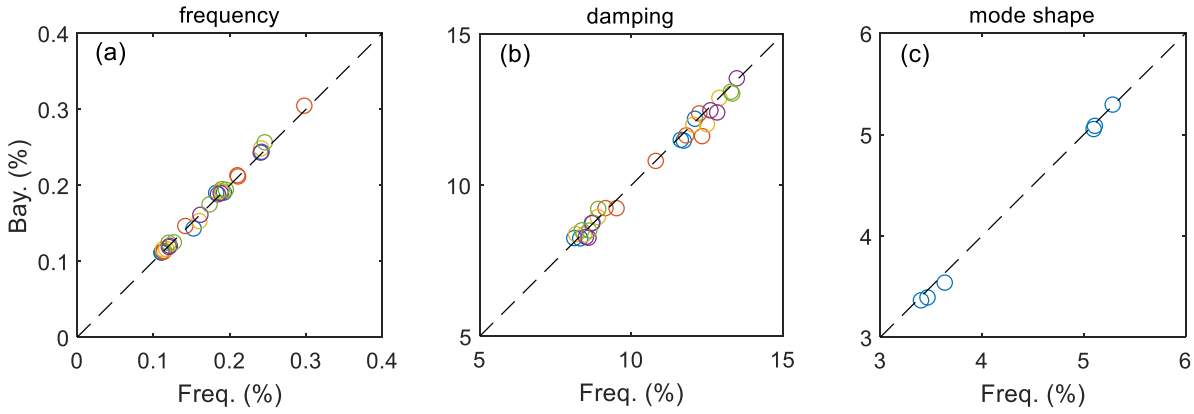

Fig. 7 Comparison of Bayesian and frequentist statistics

4.4 Effect of reference sensor location

Planning the location of reference sensors is a basic essential task in a multiple-setup test. This section investigates how the quality of identification results depends on the reference sensor location through a parametric study. For this purpose, five cases are considered here. In each case, the reference sensor is placed on different floors, from Location 11 at Level 1 in the first case to Location 15 at Level 5 in the fifth case. In each case, the roving sensors move in the same way in different setups as before (see Fig. 1(b)). Fig. 8 shows the mode shape c.o.v. versus reference sensor location for different modes. It is seen that the mode shape c.o.v. of Modes TX1, TY1 and R1 tend to be smaller when the reference sensor is placed on the higher floor. As evidenced by the mode shapes in Fig. 4, the vibration level of these modes increases with the floor number. Intuitively, placing the reference sensors at the higher floor provides better quality information to be shared among different setups, hence improving the identification precision of the identified mode shapes. On the other hand, when the reference sensor is placed at Level 4, the mode shape c.o.v. of Modes TX2, TY2 and R2 are significantly higher than their counterparts in other cases (around 4%). Fig. 9 shows the singular value spectrum based on the data collected at Level 4. It is seen that the resonance band dominated by Modes TX2 and TY2 is significantly narrower compared to that in Fig. 2 (based on the data at Level 5) and the peaks are closer to the noise level, indicating lower modal s/n ratios for both modes. The resonance peak of Mode R2 is even 'buried' by the noise and cannot be detected from the spectrum. The low modal s/n ratio at the reference location (which may be unknown prior to the test) increases the posterior uncertainty of the identified mode shapes.

In full-scale vibration tests, one often determines the reference sensor location(s) based on experience. Whenever possible, a pre-test can be done to collect data at the possible reference locations. The measured data can then be used to obtain the s/n ratios of the modes of interest.

Generally, determining the reference location(s) is a trade-off among the s/n ratios of the modes of interest since a location that has a high s/n ratio for one mode need not be so for another. E.g., the midspan of a bridge is the location that has the highest s/n ratio for the first vertical mode, but it is the node of the second mode. In practice, for robustness a common strategy in full-scale vibration tests is to have more reference locations. Of course, this is at the expense of reducing the number of rover sensors, which may in turn require more setups.

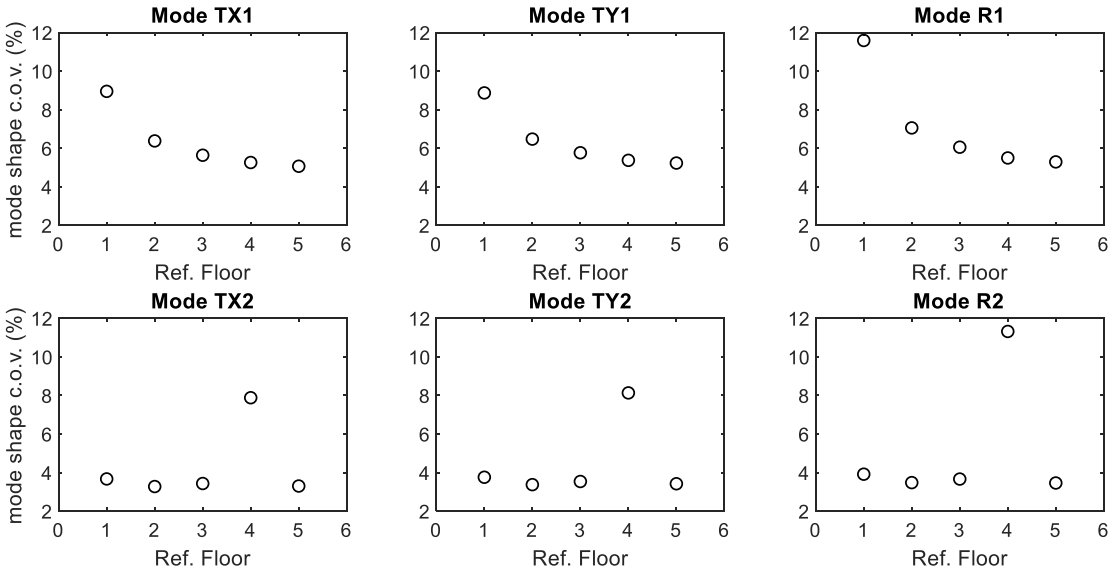

Fig. 8 Mode shape c.o.v. versus reference sensor location for different modes

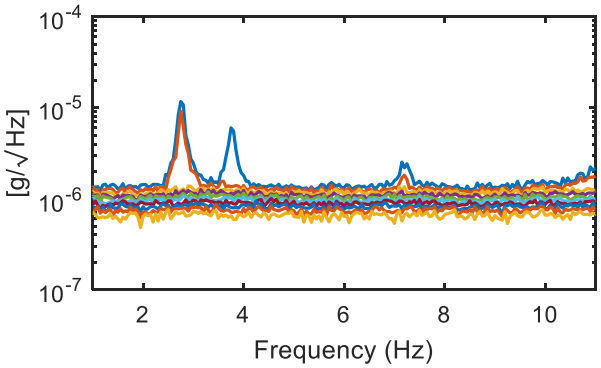

Fig. 9 Singular value spectrum based on the data collected at Level 4

We next investigate how the reference sensor location affects the identified natural frequencies and damping ratios. Fig. 10 shows the identified natural frequencies and damping ratios of Mode TX1 versus reference sensor location. The results for each case are reported with a dot at the MPV and an error bar covering ±2 posterior standard deviation. The blue line indicates the exact value. It is seen that the posterior c.o.v. of the modal parameters in Setup 1 decrease with the reference floor number, although to a lesser extent compared to mode shape c.o.v.. Note that the roving sensors in Setup 1 are placed at Level 1. Putting the reference sensor at a

higher floor can increase the modal s/n ratio in this setup, hence decreasing the identification uncertainty. The posterior c.o.v. in other setups are insensitive to the reference sensor location, as reflected by error bars of similar lengths. This is because the data measured by the roving sensors in these setups already contributes to a sufficiently high modal s/n ratio; putting the reference at higher floors has a diminishing marginal effect in reducing the identification uncertainty of natural frequency or damping ratio. This is consistent with the saturating behaviour of the posterior c.o.v. to modal s/n ratio, as revealed by uncertainty law [43]. The results for Modes TY1 and R1 (omitted here) are qualitatively similar.

Fig. 11 shows the identified natural frequencies and damping ratios of Modes TX2 and R2 in Setup 4 (where the roving sensors are placed at Level 4). The results in other setups are insensitive to the reference location and omitted here. The results of TY2 (omitted here) are qualitatively similar to those of TX2. It is seen that the posterior uncertainties are significantly higher when the reference sensor is placed at Level 4 because the data measured by all the sensors in Setup 4 has low s/n ratios for these modes in this case (see Fig. 9). Significant departure can be observed for the identified damping ratio of Mode R2 in Setup 4, with the MPV and posterior c.o.v. being 7% and 84%, respectively.

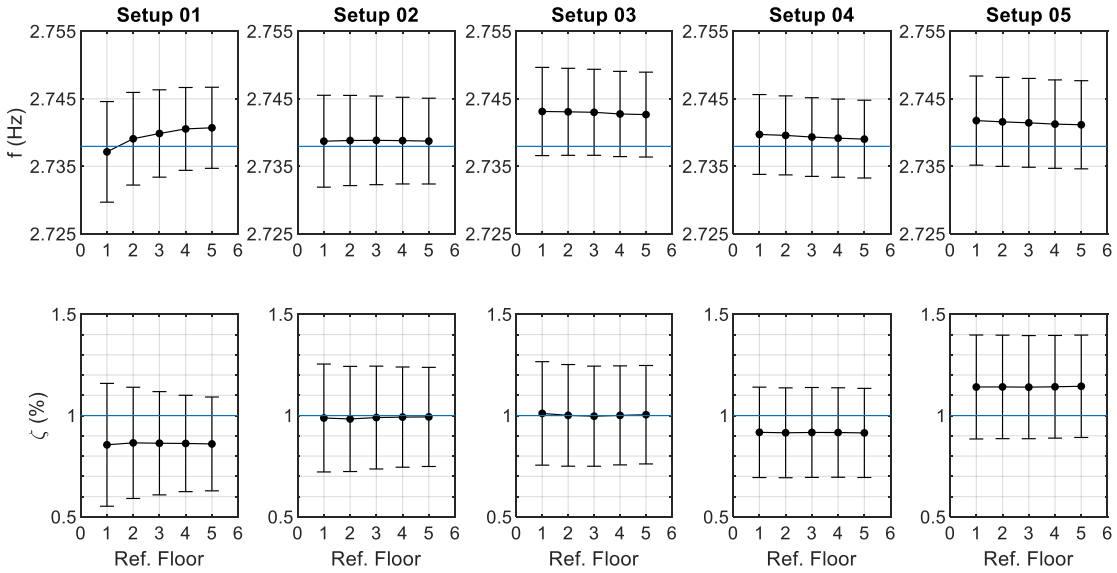

Fig. 10 Identified natural frequencies and damping ratios of Mode TX1 versus reference sensor location. Blue line - exact value; dot: MPV; error bar: ±2 posterior standard deviation

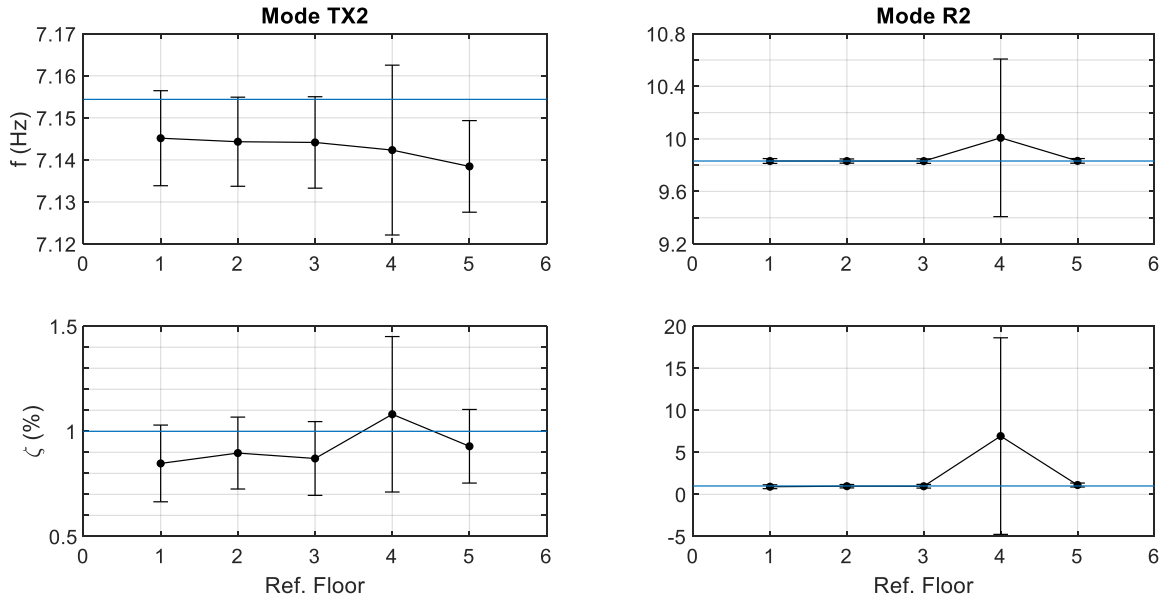

Fig. 11 Identified natural frequencies and damping ratios of Modes TX2 and R2 in Setup 4 versus reference sensor location. Blue line - exact value; dot: MPV; error bar: ±2 posterior standard deviation

5 Application to field data (Jiangyin Bridge)

The developed theory and computational algorithms are next applied to Jiangyin Bridge over the Yangtze River in China [5], see Fig. 12(a). It is a suspension bridge with a main span of 1385 m and connects Jiangyin south of the river to Jingjiang to the North. One may refer to [45] for the information on the design and construction of the bridge. An ambient vibration test was carried out from 26th to 28th April 2017. Thirteen setups were designed to cover 28 locations in total. The detailed plan can be found in Table 1 of [5]. Setups 1 - 5, Setups 6A – 6F and Setups 7 – 8 were performed on the first, second and third test day, respectively. Most of the measured locations are distributed on the east side of the bridge while the remaining ones are on the west side (to capture the torsional modes) and the tower (to characterise the tower component of deck girder modes). The two reference locations were selected near the quarter main span on the east side. In each setup, 3200s data was collected at a sampling rate of 25.6 Hz and used for analysis.

In [5], modal properties of the first twenty modes in each setup were identified separately based on a Bayesian single-setup algorithm [36,46], and the global mode shapes were assembled using the global least squares method [20]. With a Bayesian multiple-setup algorithm developed previously for MPV [27] and in this work for posterior uncertainty, the modes have also been analysed. The results are generally consistent with those in [5] and are omitted here. The discussion here focuses on some close modes at higher frequencies. Fig. 12(b) shows the singular value spectrum of the data in Setup 1. Six modes are identified here. These modes

have also been used to verify the uncertainty laws of close modes in [44] based on the data measured at the reference locations. The selected bands in this work are the same as those in [44], as indicated by the horizontal bars in Fig. 12(b).

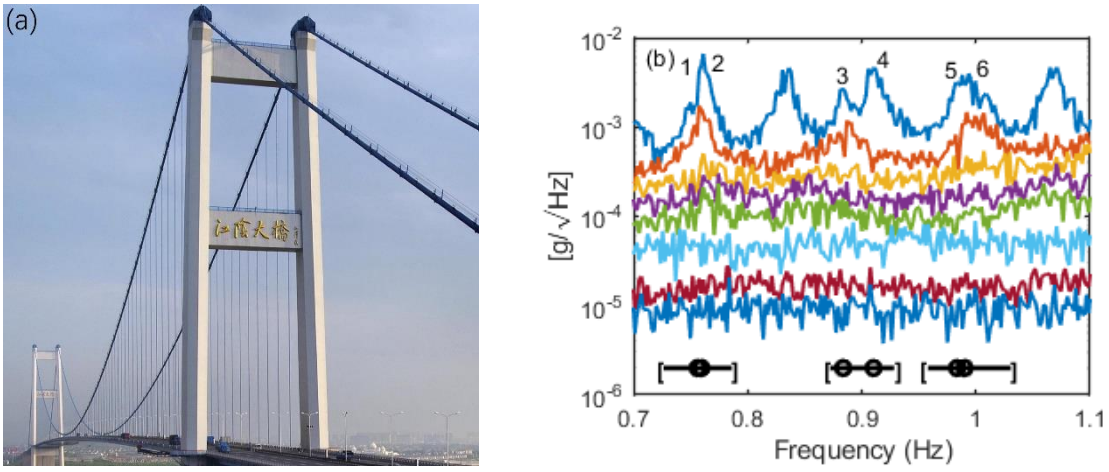

Fig. 12 (a) Jiangyin Bridge [5]; (b) singular value spectrum of Setup 1

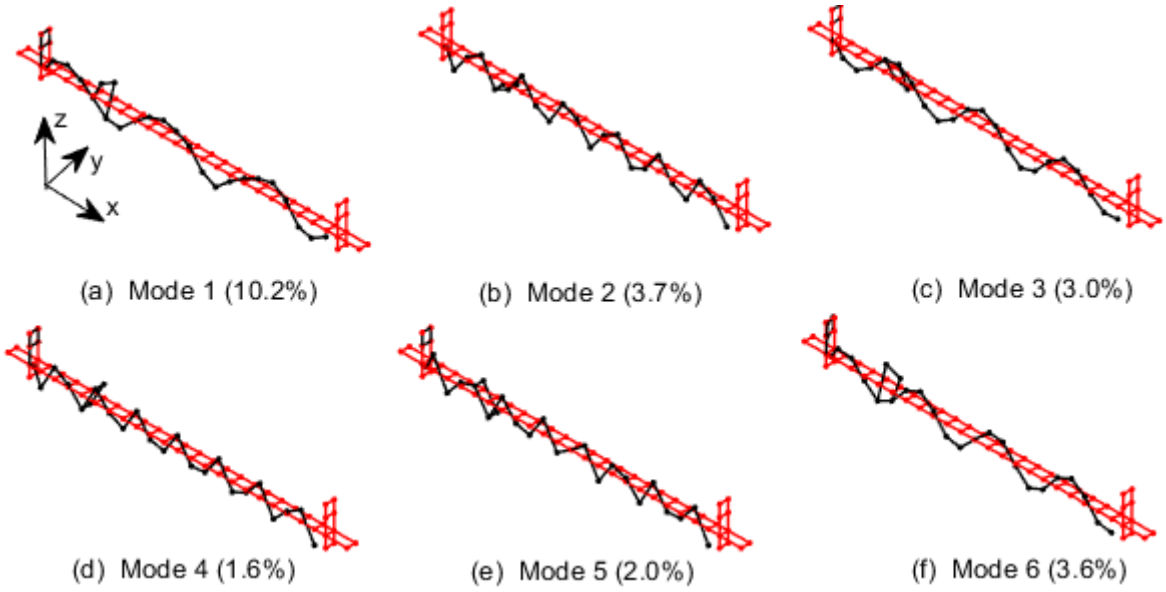

Fig. 13 Identified (most probable) mode shapes; mode shape c.o.v. in parenthesis

Fig. 13 shows the identified (most probable) mode shapes where the red and black lines indicate the undeformed and deformed shapes, respectively. The posterior mode shape c.o.v. is also reported in the figure. Modes 1, 3 and 6 are torsional modes while others are vertical modes. The mode shape uncertainty of Mode 1 (10.2%) is significantly higher than those of others (< 5%). Fig. 14 shows the identified natural frequencies and damping ratios among the setups. Both the MPVs (dots) and uncertainties (error bars) vary from one setup to another. A clear increase can be observed for the natural frequencies from Setups 5 to 6A. Note that Setup 5 is

the last setup performed on the first day while Setup 6A is the first setup on the second day. The variation of the identification results over setups could be due to the change of environment. Interestingly, the natural frequencies of Mode 1 are greater than those of Mode 2 in Setups 6A and 6C, i.e., Modes 1 and 2 are swapped in the two setups. This is not common but can occur especially for close modes. Since the Bayesian multiple-setup method directly optimises all the modal parameters based on the data, the algorithm still applies for such case without the need to match the modes in different setups manually. Table 3 summarises the sample and posterior c.o.v. of the identified modal parameters. The rows with the title of 'Freq. (%)' and 'Bay. (%)' are defined in a similar manner as Fig. 7(a) except that they are now calculated based on the data among different setups. These results serve to compare the frequentist and Bayesian statistics with the real data. It is seen that the sample c.o.v. is generally larger than posterior c.o.v., especially for modal force PSD and prediction error PSD. This is because the posterior c.o.v. reflects only identification uncertainty while the sample c.o.v. reflects both the variability of modal parameters (due to, e.g., environment change) and the identification uncertainty.

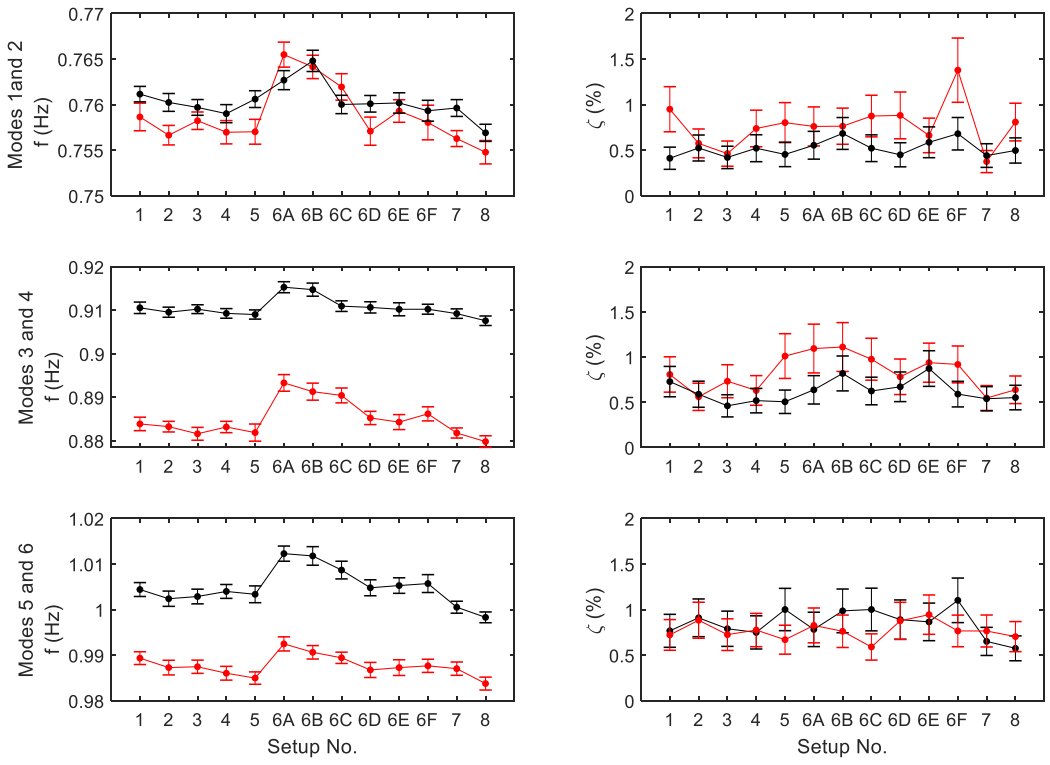

Fig. 14 Identified natural frequencies and damping ratios among the setups. Dot - MPV; error bar: ±2 posterior standard deviation. Red line - lower mode in the band; black line - higher mode in the band

Table 3 Sample and posterior c.o.v. of identified modal parameters among different setups

	Mode	1	2	3	4	5	6
f	Freq. (%)	0.41	0.23	0.45	0.24	0.23	0.41

	Bay. (%)	0.08	0.07	0.10	0.07	0.08	0.08
ζ	Freq. (%)	31	17	31	17	14	19
	Bay. (%)	15	15	13	13	12	12
S_{ii}	Freq. (%)	42	17	21	14	13	21
	Bay. (%)	16	12	11	9	10	11
S_e	Freq. (%)	42		50		53	
	Bay. (%)	4		3		3	

A previous study [27] revealed that the Bayesian multiple-setup algorithm is more robust to data quality compared to other existing methods. Fig. 15 compares the identified mode shapes of Modes 1 and 2 by the Bayesian multiple-setup algorithm and the global least squares method based on Bayesian single-setup algorithm (i.e., the method used in the analysis of [5]). Note that the latter method requires one to first match the modes manually in different setups (based on, e.g., the MAC between the mode shape values at the reference locations) before assembling the local mode shapes to form the global one. For Mode 1, the mode shape identified by the latter method is 'noiser' with kinks at some measured locations while the Bayesian multiple-setup algorithm gives a more physically reasonable mode shape. The mode shape of Mode 2 identified by both methods are consistent. This is also the case for Modes 3-6 (omitted here). Taking the identified mode shapes by Bayesian multiple-setup algorithm as a benchmark, Fig. 16 shows the MAC between the mode shape values at the reference DOFs by the Bayesian single-setup method and Bayesian multiple-setup algorithm among different setups. The MAC values of Mode 2 (red dots) are generally close to 1 in all setups except that in Setup 6E. For Mode 1 (black dots), differences do exist in some setups, e.g., Setups 4, 6B and 6F. The MAC in Setup 6B is only around 0.25, departing significantly from 1. Such inconsistency leads to challenges when assembling the mode shape of Mode 1 by the global least squares method.

Fig. 17 compares the MPV and posterior c.o.v. of natural frequencies and damping ratios of Modes 1 and 2 by the Bayesian multiple-setup algorithm and Bayesian single-setup algorithm (as is done in [5]). Generally, the results obtained by the two methods are consistent. Clear differences exist in the damping ratios of both modes in Setups 6B and 6E; the uncertainties calculated by the proposed algorithm (black error bars) are smaller than those by the Bayesian single-setup algorithm (red error bars). This is because the mode shape values at the reference locations of the two setups do not agree with those of other setups. The proposed algorithm calculates the uncertainty by analysing the data in different setups together and hence may

provide additional information from other setups. For Mode 2 in Setup 6B, the posterior c.o.v. of damping ratio calculated by the proposed algorithm is smaller than that by the Bayesian single-setup algorithm, although the mode shape values at the reference locations agree with those in other setups (see Fig. 16). This could be relevant to the entangled effect from Mode 1 as they are quite close in this setup.

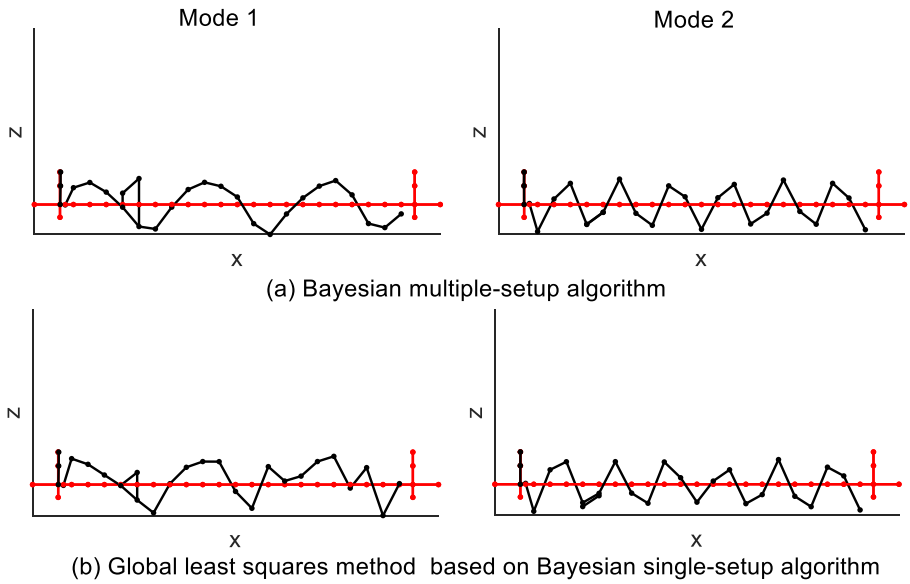

Fig. 15 Comparison of global mode shapes of Modes 1 and 2 by different methods

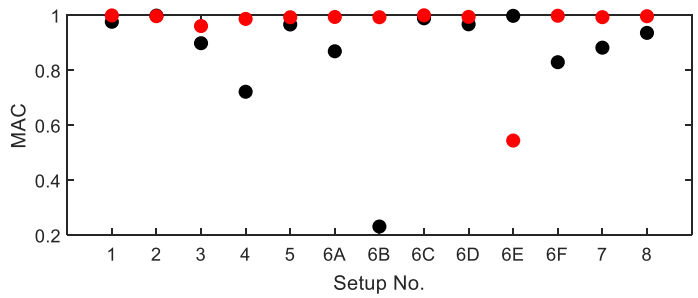

Fig. 16 MAC between the mode shape values at the reference locations using the Bayesian single-setup and multiple-setup algorithm. Black dot: Mode 1; Red dot: Mode 2

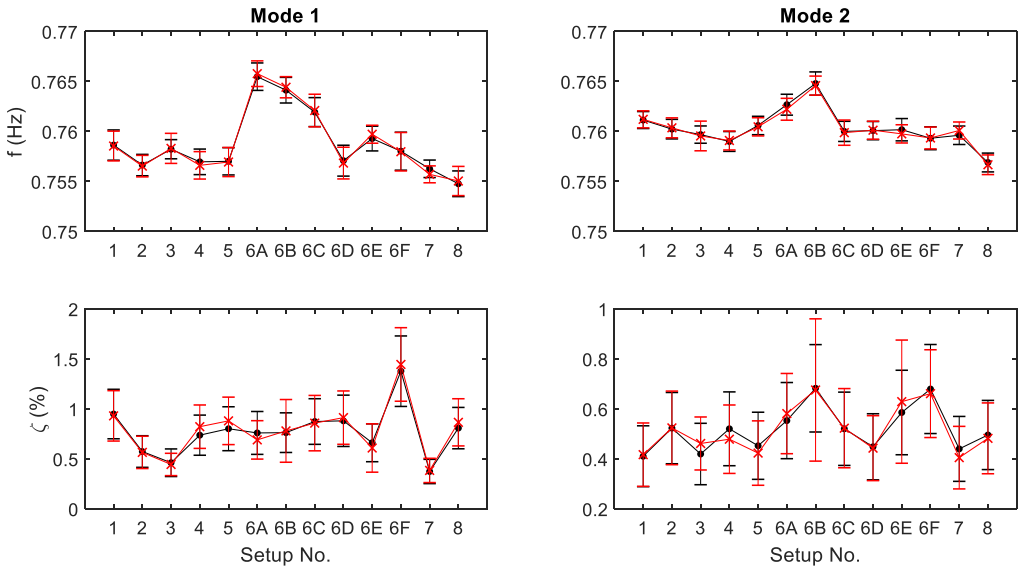

Fig. 17 Comparison of identified natural frequencies and damping ratios by Bayesian single-setup and multiple-setup algorithm. Red: single-setup algorithm; black: multiple-setup algorithm

6 Conclusions

For the general case with multiple (possibly close) modes and multiple setups, this paper presents the work on uncertainty quantification of the modal parameters identified by a recently developed Bayesian algorithm. Computational issues arising from the norm constraints on the mode shapes in the calculation of the Hessian of negative log-likelihood function and its pseudo-inverse have been addressed. Analytical expressions have been derived for the posterior covariance matrix, allowing one to quantitatively assess the precision of the identified results in an efficient and accurate manner. The proposed method has been verified using synthetic data and applied to field data.

In the synthetic example where there is no modelling error, the MPVs obtained based on i.i.d. trials can be well fitted by a Gaussian distribution with the mean close to the 'exact' values that generate the data. The posterior uncertainty in a Bayesian context is consistent with that in a frequentist context. The effect of reference location on the identification uncertainty has also been investigated. The mode shape c.o.v. generally decreases with increasing modal s/n ratio at the reference locations. The posterior c.o.v. of other parameters are less sensitive to the reference location as long as the modal s/n ratio at the roving sensor locations in the corresponding setup can be managed to an adequate level. A difficult situation in practice was considered where the reference location and all the roving sensors in a particular setup were placed at the nodes of some modes. In this case, the quality of the identified results in the

corresponding setup has significantly higher posterior uncertainty since there is no sufficient information for the inference.

The proposed algorithm has been applied to the ambient vibration data of Jiangyin bridge, focusing on some challenging close modes. The order of modes changed in some setups, which is sometimes observed in multiple-setup tests for close modes. Nevertheless, the Bayesian multiple-setup method is still applicable for such case without the need to match the modes among the setups manually as far as the modes in the same band are concerned. Comparison between the Bayesian single-setup method and the proposed algorithm shows that the identification results by the two methods are generally consistent when the modal s/n ratio is high in all setups. Difference exists when the data quality in some setups is poor. Incorporating multiple setup data by the proposed method can reduce the posterior uncertainty, by virtue of incorporating additional information available from other setups for inference. Since the Bayesian multiple-setup algorithm developed in [27] (for determining the MPV) and the proposed algorithm in this work (for uncertainty quantification) focus on the general scenario with multiple setups and multiple modes, they are also applicable for the special cases developed before, e.g., well-separated modes with single setup or multiple setup data, and close modes with single setup data.

7 Acknowledgements

This work is funded by the UK Engineering & Physical Sciences Research Council (EP/N017897/1). The majority of the work was performed during the PhD study of the first author supported by the Joint University of Liverpool/China Scholarship Council Scholarship. The thesis can be found in [47]. The second author is currently supported by grant SUG/4 (C120032000) at the Nanyang Technological University, Singapore. The financial supports are gratefully acknowledged. The authors would like to thank Prof. James Brownjohn at the University of Exeter for providing the Jiangyin Bridge field data.

8 Supplementary data

The synthetic data and computer code for implementing the Bayesian method is available upon request by contacting zuo.zhu@hotmail.com.

9 Appendix A the derivatives of $L(\boldsymbol{\theta})$ w.r.t. ϖ

In this appendix, we derive the derivatives of $L(\boldsymbol{\theta})$ in (18) w.r.t. ϖ. Clearly, for any parameters x and y in ϖ,

$$L^{(x)} = L_e^{(x)} + L_J^{(x)} + L_H^{(x)} + L_Q^{(x)} \qquad L^{(xy)} = L_e^{(xy)} + L_J^{(xy)} + L_H^{(xy)} + L_Q^{(xy)} \tag{31}$$

where the superscripted symbol '$^{(x)}$' and '$^{(xy)}$' denote the derivatives w.r.t. the corresponding variables. Then the derivatives of L can be separated into four parts.

Derivatives of L_e

Since L_e depends only on $S_e^{(r)}$ $(r = 1, \cdots, n_s)$, the derivatives are non-zero only when taken w.r.t. $S_e^{(r)}$:

$$L_e^{\left(S_e^{(r)}\right)} = \left(n_r - m\right) N_f^{(r)} S_e^{(r)-1} \quad L_e^{\left(S_e^{(r)} S_e^{(r)}\right)} = -\left(n_r - m\right) N_f^{(r)} S_e^{(r)-2} \tag{32}$$

Derivatives of L_H

For any parameter x and y in Setup r other than mode shapes:

$$L_H^{(x)} = \sum_k \left(\ln\left|\mathbf{H}_k^{(r)}\right|\right)^{(x)} \quad L_H^{(xy)} = \sum_k \left(\ln\left|\mathbf{H}_k^{(r)}\right|\right)^{(xy)} \tag{33}$$

The derivatives of $\ln\left|\mathbf{H}_k^{(r)}\right|$ can be expressed in terms of the derivatives of $\mathbf{H}_k^{(r)}$:

$$\begin{aligned} \left(\ln\left|\mathbf{H}_k^{(r)}\right|\right)^{(x)} &= tr\left[\mathbf{H}_k^{(r)-1}\left(\mathbf{H}_k^{(r)}\right)^{(x)}\right] \\ \left(\ln\left|\mathbf{H}_k^{(r)}\right|\right)^{(xy)} &= tr\left[\mathbf{H}_k^{(r)-1}\left(\mathbf{H}_k^{(r)}\right)^{(xy)} - \left(\mathbf{H}_k^{(r)}\right)^{-1}\left(\mathbf{H}_k^{(r)}\right)^{(x)}\left(\mathbf{H}_k^{(r)}\right)^{-1}\left(\mathbf{H}_k^{(r)}\right)^{(y)}\right] \end{aligned} \tag{34}$$

The derivatives of $\mathbf{H}_k^{(r)}$ are given in Table 4. The expressions depend on the derivatives of the transfer function $h_{ik}^{(r)}$ (i = 1, 2, …, m), which are given in Table 5 [1].

Derivatives of L_J

The derivation for the derivatives of L_J is similar to that of L_H. For any parameter x and y in Setup r other than mode shape:

$$L_J^{(x)} = \sum_k \left(\ln \left| \mathbf{J}_k^{(r)} \right| \right)^{(x)} \quad L_J^{(xy)} = \sum_k \left(\ln \left| \mathbf{J}_k^{(r)} \right| \right)^{(xy)} \tag{35}$$

The derivatives of $\ln \left| \mathbf{J}_k^{(r)} \right|$ can be obtained in a similar way as the derivatives of $\ln \left| \mathbf{H}_k^{(r)} \right|$ using (34) (replacing $\mathbf{H}_k^{(r)}$ by $\mathbf{J}_k^{(r)}$) in terms of the derivatives of $\mathbf{J}_k^{(r)}$. The latter are given in Table 6, where the derivatives of $\mathbf{H}_k^{(r)-1}$ can be expressed in terms of $\mathbf{H}_k^{(r)}$:

$$\begin{aligned} \left(\mathbf{H}_k^{(r)-1} \right)^{(x)} &= -\mathbf{H}_k^{(r)-1} \left(\mathbf{H}_k^{(r)} \right)^{(x)} \mathbf{H}_k^{(r)-1} \\ \left(\mathbf{H}_k^{(r)-1} \right)^{(xy)} &= \mathbf{H}_k^{(r)-1} \left[\left(\mathbf{H}_k^{(r)} \right)^{(y)} \mathbf{H}_k^{(r)-1} \left(\mathbf{H}_k^{(r)} \right)^{(x)} + \left(\mathbf{H}_k^{(r)} \right)^{(x)} \mathbf{H}_k^{(r)-1} \left(\mathbf{H}_k^{(r)} \right)^{(y)} - \left(\mathbf{H}_k^{(r)} \right)^{(xy)} \right] \mathbf{H}_k^{(r)-1} \end{aligned} \tag{36}$$

Derivatives of L_Q

The derivatives of L_Q are given in Table 7 in terms of the derivatives of $Q^{(r)}$.

For any parameter x and y in Setup r other than the mode shape:

$$\left(Q^{(r)} \right)^{(x)} = \sum_k \mathbf{s}_k^{(r)*} \left(\mathbf{J}_k^{(r)-1} \right)^{(x)} \mathbf{s}_k^{(r)} \qquad \left(Q^{(r)} \right)^{(xy)} = \sum_k \mathbf{s}_k^{(r)*} \left(\mathbf{J}_k^{(r)-1} \right)^{(xy)} \mathbf{s}_k^{(r)} \tag{37}$$

where the derivatives of $\mathbf{J}_k^{(r)-1}$ can be obtained by (36) (replacing $\mathbf{H}_k^{(r)}$ by $\mathbf{J}_k^{(r)}$) in terms of the derivatives of $\mathbf{J}_k^{(r)}$.

Table 4 Derivatives of $\mathbf{H}_k^{(r)} = \mathbf{h}_k^{(r)} \mathbf{S}^{(r)} \mathbf{h}_k^{(r)*}$

$\left(\mathbf{H}_k^{(r)}\right)^{(xy)}$		$y =$		
		$f_j^{(r)},\ \zeta_j^{(r)}$	$S_{jj}^{(r)}$	$U_{ts}^{(r)},\ V_{ts}^{(r)}$
$x =$	$f_i^{(r)},\ \zeta_i^{(r)}$	$\left[\left(h_{jk}^{(r)}\right)^{(y)*}\left(h_{1k}^{(r)}\right)^{(x)*} S_{ij}^{(r)}\mathbf{e}_{ij} + \delta_{ij}\left(h_{jk}^{(r)}\right)^{(xy)*}\mathbf{h}_k^{(r)}\mathbf{S}^{(r)}\mathbf{e}_{jj}\right] + (\bullet)^*$	$\delta_{ij}\left(h_{jk}^{(r)}\right)^{(x)} h_{jk}^{(r)*}\mathbf{e}_{jj} + (\bullet)^*$	$c\left(h_{tk}^{(r)}\right)^{(x)} h_{sk}^{(r)*}\mathbf{e}_{ts} + (\bullet)^* \quad i = t$ $ch_{tk}^{(r)}\left(h_{sk}^{(r)*}\right)^{(x)}\mathbf{e}_{ts} + (\bullet)^* \quad i = s$
	$S_{ii}^{(r)}$		**0**	**0**
	$U_{ij}^{(r)},\ V_{ij}^{(r)}$	Sym.		**0**
$\left(\mathbf{H}_k^{(r)}\right)^{(y)}$		$\left(h_{jk}^{(r)}\right)^{(y)*}\mathbf{h}_k^{(r)}\mathbf{S}^{(r)}\mathbf{e}_{jj} + (\bullet)^*$	$h_{jk}^{(r)} h_{jk}^{(r)*}\mathbf{e}_{jj}$	$ch_{tk}^{(r)} h_{sk}^{(r)*}\mathbf{e}_{ts} + (\bullet)^*$ $c = 1$ for $U_{ts}^{(r)}$ $c = \mathbf{i}$ for $V_{ts}^{(r)}$

Notes: $\mathbf{e}_{ij}$ denotes a matrix with (i, j)-entry equal to 1 and zero otherwise

Table 5 Derivatives of $h_{ik}^{(r)} = \left(1 - \beta_{ik}^{(r)2} - 2\zeta_i^{(r)}\beta_{ik}^{(r)}\mathbf{i}\right)^{-1}$ where $\beta_{ik}^{(r)} = f_i^{(r)} / \mathrm{f}_k^{(r)}$

$\left(h_{ik}^{(r)}\right)^{(xy)}$		$y =$	
		$f_i^{(r)}$	$\zeta_i^{(r)}$
$x =$	$f_i^{(r)}$	$2\left(h_{ik}^{(r)}\right)^3\left(3\beta_{ik}^{(r)2} + 1 - 4\zeta_i^{(r)2} + 6\mathbf{i}\zeta_i^{(r)}\beta_{ik}^{(r)}\right)\mathrm{f}_k^{(r)-2}$	$2\mathbf{i}\left(3\left(\beta_{ik}^{(r)}\right)^2 + 1 + 2\mathbf{i}\zeta_i^{(r)}\beta_{ik}^{(r)}\right)\left(h_{ik}^{(r)}\right)^3\mathrm{f}_k^{(r)-1}$
	$\zeta_i^{(r)}$	Sym.	$-8\mathbf{i}\left(\beta_{ik}^{(r)}\right)^2\left(h_{ik}^{(r)}\right)^3$
$\left(h_{ik}^{(r)}\right)^{(x)}$		$2\left(\beta_{ik}^{(r)} + \mathbf{i}\zeta_i^{(r)}\right)\left(h_{ik}^{(r)}\right)^2\mathrm{f}_k^{(r)-1}$	$2\mathbf{i}\beta_{ik}^{(r)}\left(h_{ik}^{(r)}\right)^2$

Table 6 Derivatives of $\mathbf{J}_k^{(r)} = S_e^{(r)}\left(\mathbf{H}_k^{(r)}\right)^{-1} + \mathbf{\Phi}^T\mathbf{L}_r^T\mathbf{L}_r\mathbf{\Phi}$

$\left(\mathbf{J}_k^{(r)}\right)^{(xy)}$		$y =$	
		$f_j^{(r)},\ \zeta_j^{(r)}, S_{jj}^{(r)}, U_{ts}^{(r)},\ V_{ts}^{(r)}$	$S_e^{(r)}$
$x =$	$f_i^{(r)},\ \zeta_i^{(r)}, S_{ii}^{(r)}, U_{ij}^{(r)},\ V_{ij}^{(r)}$	$S_e^{(r)}\left(\mathbf{H}_k^{(r)-1}\right)^{(xy)}$	$\left(\mathbf{H}_k^{(r)-1}\right)^{(x)}$
	$S_e^{(r)}$	Sym.	$\mathbf{0}$
$\left(\mathbf{J}_k^{(r)}\right)^{(y)}$		$S_e^{(r)}\left(\mathbf{H}_k^{(r)-1}\right)^{(y)}$	$\mathbf{H}_k^{(r)-1}$

Table 7 Derivatives of $L_Q = \sum_{r=1}^{n_s} S_e^{(r)-1}\left(d^{(r)} - Q^{(r)}\right)$

$\left(L_Q\right)^{(xy)}$		$y =$	
		$f_j^{(r)},\ \zeta_j^{(r)}, S_{jj}^{(r)},$ $U_{ts}^{(r)},\ V_{ts}^{(r)}$	$S_e^{(r)}$
$x =$	$f_j^{(r)},\ \zeta_j^{(r)}, S_{jj}^{(r)},$ $U_{ts}^{(r)},\ V_{ts}^{(r)}$	$-S_e^{(r)-1}\left(Q^{(r)}\right)^{(xy)}$	$S_e^{(r)-2}\left(Q^{(r)}\right)^{(x)} - S_e^{(r)-1}\left(Q^{(r)}\right)^{\left(xS_e^{(r)}\right)}$
	$S_e^{(r)}$	Sym.	$2S_e^{(r)-3}\left(d^{(r)} - Q^{(r)}\right)$ $+2S_e^{(r)-2}\left(Q^{(r)}\right)^{\left(S_e^{(r)}\right)} - S_e^{(r)-1}\left(Q^{(r)}\right)^{\left(S_e^{(r)}S_e^{(r)}\right)}$
$\left(L_Q\right)^{(y)}$		$-S_e^{(r)-1}\left(Q^{(r)}\right)^{(x)}$	$-S_e^{(r)-2}\left(d^{(r)} - Q^{(r)}\right) - S_e^{(r)-1}\left(Q^{(r)}\right)^{\left(S_e^{(r)}\right)}$

In summary, Fig. 18 illustrates the information flow of derivative calculations w.r.t. ϖ .

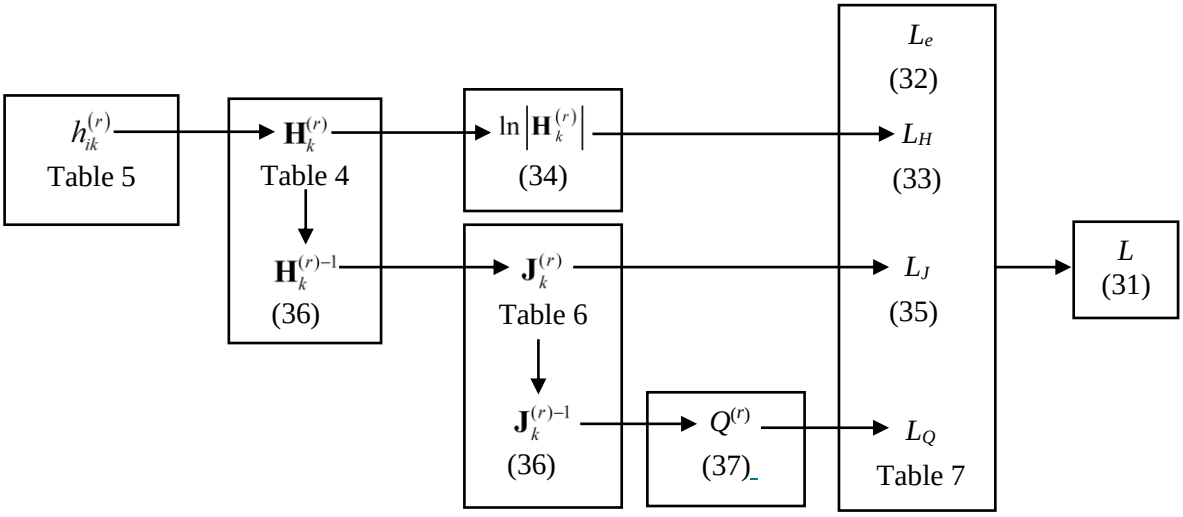

Fig. 18 Information flow of derivative calculations w.r.t. ϖ

10 Appendix B the gradient of $L(\boldsymbol{\theta})$ w.r.t. $\boldsymbol{\Phi}$

This appendix derives the condensed form of the gradient of L w.r.t. $\boldsymbol{\Phi}$. First note that $\boldsymbol{\Phi}$ is only involved in L_J and L_Q in (18). Hence, the main task is to determine $\partial L_J/\partial\boldsymbol{\Phi}$ and $\partial L_Q/\partial\boldsymbol{\Phi}$. Let Φ_{ij} denotes the (i, j)-entry of $\boldsymbol{\Phi}$. Taking the derivatives of L_J w.r.t. Φ_{ij} and using (34) (replacing $\mathbf{H}_k^{(r)}$ by $\mathbf{J}_k^{(r)}$) gives

$$\begin{aligned}\frac{\partial L_J}{\partial \Phi_{ij}} &= \sum_{r=1}^{n_s}\sum_k tr\left[\mathbf{J}_k^{(r)-1}\left(\mathbf{J}_k^{(r)}\right)^{(\Phi_{ij})}\right] = \sum_{r=1}^{n_s}\sum_k tr\left[\mathbf{J}_k^{(r)-1}\left(\boldsymbol{\Phi}^T\mathbf{A}_r e_i e_j^T + e_j e_i^T\mathbf{A}_r\boldsymbol{\Phi}\right)\right] \\ &= \sum_{r=1}^{n_s}\sum_k\left(e_j^T\mathbf{J}_k^{(r)-1}\boldsymbol{\Phi}^T\mathbf{A}_r e_i + e_i^T\mathbf{A}_r\boldsymbol{\Phi}\mathbf{J}_k^{(r)-1}e_j\right) = 2\sum_{r=1}^{n_s}\sum_k \mathrm{Re}\left(\mathbf{A}_r\boldsymbol{\Phi}\mathbf{J}_k^{(r)-1}\right)_{ij}\end{aligned} \tag{38}$$

where $(\bullet)_{ij}$ denotes the (i, j)-entry of the corresponding matrix and $\mathbf{A}_r = \mathbf{L}_r^T\mathbf{L}_r$. This indicates

$$\frac{\partial L_J}{\partial \boldsymbol{\Phi}} = 2\sum_{r=1}^{n_s}\sum_k \mathrm{Re}\left(\mathbf{A}_r\boldsymbol{\Phi}\mathbf{J}_k^{(r)-1}\right) \tag{39}$$

On the other hand, taking the derivatives of L_Q w.r.t. Φ_{ij} and using the cyclic property of the trace gives

$$\frac{\partial L_Q}{\partial \Phi_{ij}} = -2\sum_{r=1}^{n_s} S_e^{(r)-1}\sum_k \mathrm{Re}\left(\mathbf{e}_i^T\mathbf{D}_k^{(r)}\boldsymbol{\Phi}\mathbf{J}_k^{(r)-1}\mathbf{e}_j\right) - \sum_{r=1}^{n_s} S_e^{(r)-1}\sum_k \mathbf{s}_k^{(r)*}\left(\mathbf{J}_k^{(r)-1}\right)^{(\Phi_{ij})}\mathbf{s}_k^{(r)} \tag{40}$$

where $\mathbf{D}_k^{(r)} = \mathbf{L}_r^T \mathcal{F}_k^{(r)} \mathcal{F}_k^{(r)*} \mathbf{L}_r$. For the first term, assembling row-wise for *i* and column-wise for *j* gives the matrix $-2\sum_{r=1}^{n_s} S_e^{(r)-1} \sum_k \mathrm{Re}\left(\mathbf{D}_k^{(r)} \boldsymbol{\Phi} \mathbf{J}_k^{(r)-1}\right)$. Substituting $\mathbf{s}_k^{(r)} = \boldsymbol{\Phi}^T \mathbf{L}_r^T \mathcal{F}_k^{(r)}$ into the second term and noting $\left(\mathbf{J}_k^{(r)-1}\right)^{(\Phi_{ij})} = -\mathbf{J}_k^{(r)-1} \left(\mathbf{J}_k^{(r)}\right)^{(\Phi_{ij})} \mathbf{J}_k^{(r)-1}$, one can obtain

$$
\begin{aligned}
&-\sum_{r=1}^{n_s} S_e^{(r)-1} \sum_k \mathbf{s}_k^{(r)*} \left(\mathbf{J}_k^{(r)-1}\right)^{(\Phi_{ij})} \mathbf{s}_k^{(r)} = \sum_{r=1}^{n_s} S_e^{(r)-1} \sum_k \mathbf{s}_k^{(r)*} \mathbf{J}_k^{(r)-1} \left(\mathbf{J}_k^{(r)}\right)^{(\Phi_{ij})} \mathbf{J}_k^{(r)-1} \mathbf{s}_k^{(r)} \\
&= \sum_{r=1}^{n_s} S_e^{(r)-1} \sum_k \mathbf{s}_k^{(r)*} \mathbf{J}_k^{(r)-1} \left(\boldsymbol{\Phi}^T \mathbf{L}_r^T \mathbf{L}_r \mathbf{e}_i \mathbf{e}_j^T + \mathbf{e}_j \mathbf{e}_i^T \mathbf{L}_r^T \mathbf{L}_r \boldsymbol{\Phi}\right) \mathbf{J}_k^{(r)-1} \mathbf{s}_k^{(r)} \\
&= 2\sum_{r=1}^{n_s} S_e^{(r)-1} \sum_k \mathrm{Re}\left(\mathbf{e}_i^T \mathbf{A}_r \boldsymbol{\Phi} \mathbf{J}_k^{(r)-1} \boldsymbol{\Phi}^T \mathbf{D}_k^{(r)} \boldsymbol{\Phi} \mathbf{J}_k^{(r)-1} \mathbf{e}_j\right)
\end{aligned}
\tag{41}
$$

Then assembling this term row-wise for *i* and column-wise for *j* gives the matrix $2\sum_{r=1}^{n_s} S_e^{(r)-1} \sum_k \mathrm{Re}\left(\mathbf{A}_r \boldsymbol{\Phi} \mathbf{J}_k^{(r)-1} \boldsymbol{\Phi}^T \mathbf{D}_k^{(r)} \boldsymbol{\Phi} \mathbf{J}_k^{(r)-1}\right)$. Combing the first and second term gives

$$
\frac{\partial L_Q}{\partial \boldsymbol{\Phi}} = -\sum_{r=1}^{n_s} 2 S_e^{(r)-1} \,\mathrm{Re}\left[\sum_k \left(\mathbf{D}_k^{(r)} \boldsymbol{\Phi} \mathbf{J}_k^{(r)-1} - \mathbf{A}_r \boldsymbol{\Phi} \mathbf{J}_k^{(r)-1} \boldsymbol{\Phi}^T \mathbf{D}_k^{(r)} \boldsymbol{\Phi} \mathbf{J}_k^{(r)-1}\right)\right] \tag{42}
$$

Combining (39) and (42), and after rearranging, one can obtain (24).

11 Appendix C Cross derivatives of $L(\boldsymbol{\theta})$ w.r.t. ϖ and $vec(\boldsymbol{\Phi})$

In this appendix, we derive the cross derivatives of $L(\boldsymbol{\theta})$ in (18) w.r.t. ϖ and $vec\left(\boldsymbol{\Phi}\right)$, i.e., the derivatives of $\partial L / \partial vec\left(\boldsymbol{\Phi}\right)^T$ in (24) w.r.t. ϖ. The following identities [48] will be used for the computation:

For any matrix **Y** (*p*-by-*q*) and **Z** (*q*-by-*r*), which depend on matrix **X** (*s*-by-*t*)

$$
\underbrace{\frac{\partial vec\left(\mathbf{YZ}\right)^T}{\partial vec\left(\mathbf{X}\right)}}_{st \times pr} = \underbrace{\frac{\partial vec\left(\mathbf{Z}\right)^T}{\partial vec\left(\mathbf{X}\right)}}_{st \times qr} \underbrace{\left(\mathbf{I}_r \otimes \mathbf{Y}^T\right)}_{qr \times pr} + \underbrace{\frac{\partial vec\left(\mathbf{Y}\right)^T}{\partial vec\left(\mathbf{X}\right)}}_{st \times pq} \underbrace{\left(\mathbf{Z} \otimes \mathbf{I}_p\right)}_{pq \times pr} \tag{43}
$$

For an invertible matrix **F(X)** (*p*-*by*-*p*) which is a function of **X**

$$
\frac{\partial vec\left(\mathbf{F}\left(\mathbf{X}\right)^{-1}\right)^T}{\partial vec\left(\mathbf{X}\right)} = -\frac{\partial vec\left(\mathbf{F}\left(\mathbf{X}\right)\right)^T}{\partial vec\left(\mathbf{X}\right)} \left[\mathbf{F}\left(\mathbf{X}\right)^{-1} \otimes \mathbf{F}\left(\mathbf{X}\right)^{-T}\right] \tag{44}
$$

Note that except $S_e^{(r)}$ the modal parameters in $\boldsymbol{\varpi}$ are only involved in $\mathbf{J}_k^{(r)-1}$ in (24). First taking the derivatives of $\mathbf{U}_1$ w.r.t. $\boldsymbol{\varpi}$ and using (43) gives

$$\frac{\partial \mathbf{U}_1}{\partial \boldsymbol{\varpi}} = 2\sum_{r=1}^{n_s}\sum_{k} \mathrm{Re}\left\{ \frac{\partial vec(\mathbf{J}_k^{(r)-1})^T}{\partial \boldsymbol{\varpi}} \left[\mathbf{I}_m \otimes \left(\mathbf{A}_r \boldsymbol{\Phi} \right)^T \right] \right\} \tag{45}$$

Taking the derivatives of $\mathbf{U}_2$ w.r.t. $\boldsymbol{\varpi}$ and using (43) gives

$$\frac{\partial \mathbf{U}_2}{\partial \boldsymbol{\varpi}} = 2\sum_{r=1}^{n_s}\sum_{k} \mathrm{Re}\left\{ \frac{\partial vec\left(\mathbf{J}_k^{(r)-1} \right)^T}{\partial \boldsymbol{\varpi}} \left[\mathbf{I}_m \otimes \left(-S_e^{(r)-1} \mathbf{D}_k^{(r)} \boldsymbol{\Phi} \right)^T \right] \right\} \tag{46}$$

Similarly,

$$\begin{aligned}
\frac{\partial \mathbf{U}_3}{\partial \boldsymbol{\varpi}} &= 2\sum_{r=1}^{n_s}\sum_{k} \mathrm{Re}\left\{ \frac{\partial vec\left(\boldsymbol{\Phi}^T \mathbf{D}_k^{(r)} \boldsymbol{\Phi} \mathbf{J}_k^{(r)-1} \right)^T}{\partial \boldsymbol{\varpi}} \left[\mathbf{I}_m \otimes \left(S_e^{(r)-1} \mathbf{A}_r \boldsymbol{\Phi} \mathbf{J}_k^{(r)-1} \right)^T \right] \right\} \\
&+ 2\sum_{r=1}^{n_s}\sum_{k} \mathrm{Re}\left[\frac{\partial vec\left(S_e^{(r)-1} \mathbf{A}_r \boldsymbol{\Phi} \mathbf{J}_k^{(r)-1} \right)^T}{\partial \boldsymbol{\varpi}} \left(\boldsymbol{\Phi}^T \mathbf{D}_k^{(r)} \boldsymbol{\Phi} \mathbf{J}_k^{(r)-1} \otimes \mathbf{I}_n \right) \right] \\
&= 2\sum_{r=1}^{n_s}\sum_{k} \mathrm{Re}\left\{ \frac{\partial vec\left(\mathbf{J}_k^{(r)-1} \right)^T}{\partial \boldsymbol{\varpi}} \left[\mathbf{I}_m \otimes \left(S_e^{(r)-1} \mathbf{A}_r \boldsymbol{\Phi} \mathbf{J}_k^{(r)-1} \boldsymbol{\Phi}^T \mathbf{D}_k^{(r)} \boldsymbol{\Phi} \right)^T + \boldsymbol{\Phi}^T \mathbf{D}_k^{(r)} \boldsymbol{\Phi} \mathbf{J}_k^{(r)-1} \otimes \left(S_e^{(r)-1} \mathbf{A}_r \boldsymbol{\Phi} \right)^T \right] \right\}
\end{aligned} \tag{47}$$

When deriving (46) and (47), the effect of the term $S_e^{(r)-1}$ is ignored, which will be considered later. In (45)-(47), the term $\partial vec\left(\mathbf{J}_k^{(r)-1} \right)^T / \partial \boldsymbol{\varpi}$ is required. Based on (44),

$$\frac{\partial vec\left(\mathbf{J}_k^{(r)-1} \right)^T}{\partial \boldsymbol{\varpi}} = -\frac{\partial vec\left(\mathbf{J}_k^{(r)} \right)^T}{\partial \boldsymbol{\varpi}} \left[\mathbf{J}_k^{(r)-1} \otimes \left(\mathbf{J}_k^{(r)-T} \right) \right] \tag{48}$$

The term $\partial vec\left(\mathbf{J}_k^{(r)} \right)^T / \partial \boldsymbol{\varpi}$ can be obtained using Table 6 by stacking column-wise the columns of the derivatives of $\mathbf{J}_k^{(r)}$ and then taking the transpose.

Since $S_e^{(r)}$ is not only involved in the term $\mathbf{J}_k^{(r)-1}$, an additional term should be added together with (45)-(47) for the entries corresponding to $S_e^{(r)}$ in the cross derivative matrix, which is equal to

$$\mathbf{U}_{ad} = 2\sum_{r=1}^{n_s}\sum_{k} \mathrm{Re}\left[S_e^{(r)-2} vec\left(\mathbf{D}_k^{(r)} \boldsymbol{\Phi} \mathbf{J}_k^{(r)-1} - \mathbf{A}_r \boldsymbol{\Phi} \mathbf{J}_k^{(r)-1} \boldsymbol{\Phi}^T \mathbf{D}_k^{(r)} \boldsymbol{\Phi} \mathbf{J}_k^{(r)-1} \right)^T \right] \tag{49}$$

Then the cross derivatives of L w.r.t. ϖ and $vec(\mathbf{\Phi})$ can be obtained by summing (45)-(47) and then adding (49) with the entries corresponding to $S_e^{(r)}$ in the matrix. In summary, Fig. 19 shows the information flow of cross derivative calculations w.r.t. ϖ and $vec(\mathbf{\Phi})$.

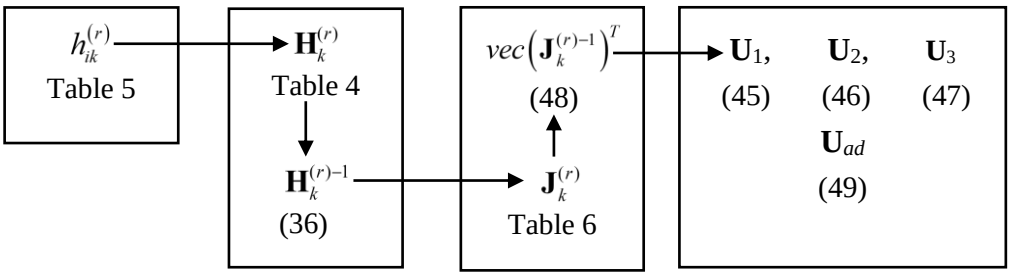

Fig. 19 Information flow of cross derivative calculations w.r.t. ϖ and $vec(\mathbf{\Phi})$

12 Appendix D Second derivatives of $L(\boldsymbol{\theta})$ w.r.t. $vec(\mathbf{\Phi})$

In this section, we derive the second derivatives of L w.r.t. $vec(\mathbf{\Phi})$, i.e., the derivative of (24) w.r.t $vec(\mathbf{\Phi})$, which is equal to the sum of the derivatives of $\mathbf{U}_1$, $\mathbf{U}_2$ and $\mathbf{U}_3$. Taking the derivatives of $\mathbf{U}_1$ in (25) w.r.t. $vec(\mathbf{\Phi})$ gives

$$\frac{\partial \mathbf{U}_1}{\partial vec(\mathbf{\Phi})} = 2\sum_{r=1}^{n_s}\sum_{k}\mathrm{Re}\left[\frac{\partial vec\left(\mathbf{\Phi}\mathbf{J}_k^{(r)-1}\right)^T}{\partial vec(\mathbf{\Phi})}\left(\mathbf{I}_m \otimes \mathbf{A}_r\right)\right] \tag{50}$$

By using (43) and (44), one can obtain

$$\frac{\partial vec\left(\mathbf{\Phi}\mathbf{J}_k^{(r)-1}\right)^T}{\partial vec(\mathbf{\Phi})} = \frac{\partial vec\left(\mathbf{J}_k^{(r)-1}\right)^T}{\partial vec(\mathbf{\Phi})}\left(\mathbf{I}_m \otimes \mathbf{\Phi}^T\right) + \mathbf{J}_k^{(r)-1} \otimes \mathbf{I}_n \tag{51}$$

and

$$\frac{\partial vec\left(\mathbf{J}_k^{(r)-1}\right)^T}{\partial vec(\mathbf{\Phi})} == -\mathbf{J}_k^{(r)-1} \otimes \left(\mathbf{A}_r\mathbf{\Phi}\mathbf{J}_k^{(r)-T}\right) - \frac{\partial vec\left(\mathbf{\Phi}^T\right)^T}{\partial vec(\mathbf{\Phi})}\left[\left(\mathbf{A}_r\mathbf{\Phi}\mathbf{J}_k^{(r)-1}\right) \otimes \mathbf{J}_k^{(r)-T}\right] \tag{52}$$

with $\partial vec\left(\mathbf{\Phi}^T\right)^T / \partial vec(\mathbf{\Phi})$ being a sparse matrix whose ($m(i$-1) + j, $n(j$-1) + i)-entry (i = 1, …, n; j = 1, …, m) is 1 and zero otherwise.

Using (23), it can be shown that $\mathbf{L}_r\boldsymbol{\Phi}\mathbf{J}_k^{(r)-1}\boldsymbol{\Phi}^T\mathbf{L}_r^T = \mathbf{I}_{n_r} - S_e^{(r)}\mathbf{E}_k^{(r)-1}$ where $\mathbf{E}_k^{(r)}$ is the theoretical PSD of the data in Setup *r*. Substituting (52) into (51) and then into (50), after rearranging, one obtains

$$\frac{\partial \mathbf{U}_1}{\partial vec(\boldsymbol{\Phi})} = 2\sum_{r=1}^{n_s}\sum_k \mathrm{Re}\left\{\mathbf{J}_k^{(r)-1}\otimes\left[\mathbf{L}_r^T\mathbf{R}_{1k}^{(r)-T}\mathbf{L}_r\right] - \frac{\partial vec\left(\boldsymbol{\Phi}^T\right)^T}{\partial vec(\boldsymbol{\Phi})}\left[\left(\mathbf{L}_r^T\mathbf{B}_k^{(r)}\right)\otimes\left(\mathbf{L}_r^T\mathbf{B}_k^{(r)}\right)^T\right]\right\} \tag{53}$$

where $\mathbf{B}_k^{(r)} = \boldsymbol{\Phi}_r\mathbf{J}_k^{(r)-1} \in C^{n_r\times m}$ and $\mathbf{R}_{1k}^{(r)} = S_e^{(r)-1}\mathbf{E}_k^{(r)} \in C^{n_r\times n_r}$. In particular, $\mathbf{R}_{1k}^{(r)}$ reflects the data s/n ratio in Setup *r*.

Taking the derivatives of $\mathbf{U}_2$ w.r.t. $vec(\boldsymbol{\Phi})$ gives

$$\frac{\partial \mathbf{U}_2}{\partial vec(\boldsymbol{\Phi})} = -2\sum_{r=1}^{n_s}\sum_k \mathrm{Re}\left[S_e^{(r)-1}\frac{\partial vec\left(\boldsymbol{\Phi}\mathbf{J}_k^{(r)-1}\right)^T}{\partial vec(\boldsymbol{\Phi})}\left(\mathbf{I}_m\otimes\mathbf{D}_k^{(r)T}\right)\right] \tag{54}$$

Substituting (51) into (54), after rearranging, one can obtain

$$\frac{\partial \mathbf{U}_2}{\partial vec(\boldsymbol{\Phi})} = 2\sum_{r=1}^{n_s}\sum_k \mathrm{Re}\left\{-\mathbf{J}_k^{(r)-1}\otimes\left(\mathbf{L}_r^T\mathbf{C}_k^{(r)T}\mathbf{L}_r\right) + \frac{\partial vec\left(\boldsymbol{\Phi}^T\right)^T}{\partial vec(\boldsymbol{\Phi})}\left[\left(\mathbf{L}_r^T\mathbf{B}_k^{(r)}\right)\otimes\left(\mathbf{B}_k^{(r)T}\mathbf{R}_{2k}^{(r)T}\mathbf{L}_r\right)\right]\right\} \tag{55}$$

where $\mathbf{C}_k^{(r)} = \mathcal{F}_k^{(r)}\mathcal{F}_k^{(r)*}\mathbf{E}_k^{(r)-1} \in C^{n_r\times n_r}$; $\mathbf{R}_{2k}^{(r)} = S_e^{(r)-1}\mathcal{F}_k^{(r)}\mathcal{F}_k^{(r)*} \in C^{n_r\times n_r}$.

Taking the derivative of $\mathbf{U}_3$ w.r.t. $vec(\boldsymbol{\Phi})$ gives

$$\frac{\partial \mathbf{U}_3}{\partial vec(\boldsymbol{\Phi})} = 2\sum_{r=1}^{n_s}\sum_k \mathrm{Re}\left[S_e^{(r)-1}\frac{\partial vec\left(\boldsymbol{\Phi}\mathbf{J}_k^{(r)-1}\boldsymbol{\Phi}^T\mathbf{D}_k^{(r)}\boldsymbol{\Phi}\mathbf{J}_k^{(r)-1}\right)^T}{\partial vec(\boldsymbol{\Phi})}\left(\mathbf{I}_m\otimes\mathbf{A}_r\right)\right] \tag{56}$$

where, by using (43),

$$\begin{aligned}\frac{\partial vec\left(\boldsymbol{\Phi}\mathbf{J}_k^{(r)-1}\boldsymbol{\Phi}^T\mathbf{D}_k^{(r)}\boldsymbol{\Phi}\mathbf{J}_k^{(r)-1}\right)^T}{\partial vec(\boldsymbol{\Phi})} &= \frac{\partial vec\left(\boldsymbol{\Phi}^T\mathbf{D}_k^{(r)}\boldsymbol{\Phi}\mathbf{J}_k^{(r)-1}\right)^T}{\partial vec(\boldsymbol{\Phi})}\left[\mathbf{I}_m\otimes\left(\boldsymbol{\Phi}\mathbf{J}_k^{(r)-1}\right)^T\right] \\ &+ \frac{\partial vec\left(\boldsymbol{\Phi}\mathbf{J}_k^{(r)-1}\right)^T}{\partial vec(\boldsymbol{\Phi})}\left(\boldsymbol{\Phi}^T\mathbf{D}_k^{(r)}\boldsymbol{\Phi}\mathbf{J}_k^{(r)-1}\otimes\mathbf{I}_n\right)\end{aligned} \tag{57}$$

In (57),

$$\frac{\partial vec\left(\boldsymbol{\Phi}^T\mathbf{D}_k^{(r)}\boldsymbol{\Phi}\mathbf{J}_k^{(r)-1}\right)^T}{\partial vec\left(\boldsymbol{\Phi}\right)}$$
$$=\frac{\partial vec\left(\boldsymbol{\Phi}\mathbf{J}_k^{(r)-1}\right)^T}{\partial vec\left(\boldsymbol{\Phi}\right)}\left[\mathbf{I}_m\otimes\left(\boldsymbol{\Phi}^T\mathbf{D}_k^{(r)}\right)^T\right]+\frac{\partial vec\left(\boldsymbol{\Phi}^T\mathbf{D}_k^{(r)}\right)^T}{\partial vec\left(\boldsymbol{\Phi}\right)}\left(\boldsymbol{\Phi}\mathbf{J}_k^{(r)-1}\otimes\mathbf{I}_m\right) \tag{58}$$
$$=\frac{\partial vec\left(\boldsymbol{\Phi}\mathbf{J}_k^{(r)-1}\right)^T}{\partial vec\left(\boldsymbol{\Phi}\right)}\left[\mathbf{I}_m\otimes\left(\boldsymbol{\Phi}^T\mathbf{D}_k^{(r)}\right)^T\right]+\frac{\partial vec\left(\boldsymbol{\Phi}^T\right)^T}{\partial vec\left(\boldsymbol{\Phi}\right)}\left(\mathbf{D}_k^{(r)}\boldsymbol{\Phi}\mathbf{J}_k^{(r)-1}\otimes\mathbf{I}_m\right)$$

Substituting (58) and (51) into (57), and then into (56), one can obtain

$$\frac{\partial\mathbf{U}_3}{\partial vec\left(\boldsymbol{\Phi}\right)}=2\sum_{r=1}^{n_s}\sum_k\mathrm{Re}\left\{\mathbf{J}_k^{(r)-1}\otimes\left[\mathbf{L}_r^T\mathbf{C}_k^{(r)T}\left(\mathbf{I}_{n_r}-\mathbf{R}_{1k}^{(r)-1}\right)\mathbf{L}_r\right]+\mathbf{B}_k^{(r)*}\mathcal{F}_k^{(r)}\mathcal{F}_k^{(r)*}\mathbf{B}_k^{(r)}\otimes\left(\mathbf{L}_r^T\mathbf{E}_k^{(r)-T}\mathbf{L}_r\right)\right\}$$
$$+2\sum_{r=1}^{n_s}\sum_k\mathrm{Re}\left\{\frac{\partial vec\left(\boldsymbol{\Phi}^T\right)^T}{\partial vec\left(\boldsymbol{\Phi}\right)}\left[\mathbf{L}_r^T\mathbf{C}_k^{(r)*}\mathbf{B}_k^{(r)}\otimes\left(\mathbf{B}_k^{(r)T}\mathbf{L}_r\right)-\left(\mathbf{L}_r^T\mathbf{B}_k^{(r)}\right)\otimes\left(\mathbf{B}_k^{(r)T}\mathbf{R}_{2k}^{(r)T}\left(\mathbf{I}_{n_r}-\mathbf{R}_{1k}^{(r)-T}\right)\mathbf{L}_r\right)\right]\right\} \tag{59}$$

Based on (53), (55) and (59), after rearranging, the second derivatives of L w.r.t. $vec\left(\boldsymbol{\Phi}\right)$ is given by (27).

13 References

[1] Au S-K. Operational modal analysis: Modeling, bayesian inference, uncertainty laws. Springer; 2017.

[2] Brincker R, Ventura CE. Introduction to Operational Modal Analysis. John Wiley & Sons; 2015.

[3] Brownjohn JMW, Magalhaes F, Caetano E, Cunha A. Ambient vibration re-testing and operational modal analysis of the Humber Bridge. Eng Struct 2010;32:2003–18.

[4] Ni Y, Lu X, Lu W. Operational modal analysis of a high-rise multi-function building with dampers by a Bayesian approach. Mech Syst Signal Process 2017;86:286–307.

[5] Brownjohn JMW, Au SK, Zhu Y, Sun Z, Li B, Bassitt J, et al. Bayesian operational modal analysis of Jiangyin Yangtze River Bridge. Mech Syst Signal Process 2018;110:210–30.

[6] Chen GW, Omenzetter P, Beskhyroun S. Operational modal analysis of an eleven-span concrete bridge subjected to weak ambient excitations. Eng Struct 2017;151:839–60.

[7] Brownjohn JMW, Raby A, Au SK, Zhu Z, Wang X, Antonini A, et al. Bayesian

operational modal analysis of offshore rock lighthouses: Close modes, alignment, symmetry and uncertainty. Mech Syst Signal Process 2019;133:106306.

[8] Lam H-F, Zhang F-L, Ni Y-C, Hu J. Operational modal identification of a boat-shaped building by a Bayesian approach. Eng Struct 2017;138:381–93.

[9] Zhang FL, Ni YC, Lam HF. Bayesian structural model updating using ambient vibration data collected by multiple setups. Struct Control Heal Monit 2017;24.

[10] Lam HF, Yang J, Au SK. Bayesian model updating of a coupled-slab system using field test data utilizing an enhanced Markov chain Monte Carlo simulation algorithm. Eng Struct 2015;102:144–55.

[11] Torres W, Almazán JL, Sandoval C, Boroschek R. Operational modal analysis and FE model updating of the Metropolitan Cathedral of Santiago, Chile. Eng Struct 2017;143:169–88.

[12] Bassoli E, Vincenzi L, D'Altri AM, de Miranda S, Forghieri M, Castellazzi G. Ambient vibration-based finite element model updating of an earthquake-damaged masonry tower. Struct Control Heal Monit 2018;25.

[13] Yin T, Jiang QH, Yuen KV. Vibration-based damage detection for structural connections using incomplete modal data by Bayesian approach and model reduction technique. Eng Struct 2017;132:260–77.

[14] Chang KC, Kim CW. Modal-parameter identification and vibration-based damage detection of a damaged steel truss bridge. Eng Struct 2016;122:156–73.

[15] Du Y, Zhou S, Jing X, Peng Y, Wu H, Kwok N. Damage detection techniques for wind turbine blades: A review. Mech Syst Signal Process 2020;141:106445.

[16] Zhang FL, Xiong HB, Shi WX, Ou X. Structural health monitoring of Shanghai Tower during different stages using a Bayesian approach. Struct Control Heal Monit 2016;23:1366–84.

[17] Zhang FL, Yang YP, Xiong HB, Yang JH, Yu Z. Structural health monitoring of a 250-m super-tall building and operational modal analysis using the fast Bayesian FFT method. Struct Control Heal Monit 2019;26:1–20.

[18] Park HS, Oh BK. Real-time structural health monitoring of a supertall building under

construction based on visual modal identification strategy. Autom Constr 2018;85:273–89.

[19] Catbas FN, Susoy M, Frangopol DM. Structural health monitoring and reliability estimation: Long span truss bridge application with environmental monitoring data. Eng Struct 2008;30:2347–59.

[20] Au SK. Assembling mode shapes by least squares. Mech Syst Signal Process 2011;25:163–79.

[21] Reynders E, Magalhães F, De Roeck G, Cunha Á. Merging strategies for multi-setup Operational Modal Analysis: Application to the Luiz i steel arch bridge. Proc. IMAC, 2009.

[22] Döhler M, Reynders E, Magalhães F, Mevel L, De Roeck G, Cunha Á. Pre- and post-identification merging for multi-setup OMA with covariance-driven SSI. Conf. Proc. Soc. Exp. Mech. Ser., 2011.

[23] Mevel L, Basseville M, Benveniste A, Goursat M. Merging sensor data from multiple measurement set-ups for non-stationary subspace-based modal analysis. J Sound Vib 2002;249:719–41.

[24] Döhler M, Mevel L. Modular subspace-based system identification from multi-setup measurements. IEEE Trans Automat Contr 2012;57:2951–6.

[25] Parloo E, Guillaume P, Cauberghe B. Maximum likelihood identification of non-stationary operational data. J Sound Vib 2003;268:971–91.

[26] Au SK, Zhang FL. Fast Bayesian Ambient Modal Identification Incorporating Multiple Setups. J Eng Mech 2012;138:800–15.

[27] Zhu Z, Au SK, Li B, Xie YL. Bayesian operational modal analysis with multiple setups and multiple (possibly close) modes. Mech Syst Signal Process 2021;150.

[28] Pintelon R, Guillaume P, Schoukens J. Uncertainty calculation in (operational) modal analysis. Mech Syst Signal Process 2007;21:2359–73.

[29] Reynders E, Pintelon R, De Roeck G. Uncertainty bounds on modal parameters obtained from stochastic subspace identification. Mech Syst Signal Process 2008;22:948–69.

[30] Döhler M, Lam XB, Mevel L. Uncertainty quantification for modal parameters from

stochastic subspace identification on multi-setup measurements. Mech Syst Signal Process 2013;36:562–81.

[31] Döhler M, Mevel L. Efficient multi-order uncertainty computation for stochastic subspace identification. Mech Syst Signal Process 2013;38:346–66.

[32] Lam XB, Mevel L. Uncertainty quantication for Eigensystem-Realization-Algorithm, a class of Subspace system Identication. IFAC Proc. Vol., 2011.

[33] Au SK, Zhang FL. On assessing the posterior mode shape uncertainty in ambient modal identification. Probabilistic Eng Mech 2011;26:427–34.

[34] Au S-K. Fast Bayesian FFT Method for Ambient Modal Identification with Separated Modes. J Eng Mech 2011;137:214–26.

[35] Zhang FL, Au SK, Lam HF. Assessing uncertainty in operational modal analysis incorporating multiple setups using a Bayesian approach. Struct Control Heal Monit 2015;22:395–416.

[36] Au SK. Fast Bayesian ambient modal identification in the frequency domain, Part II: Posterior uncertainty. Mech Syst Signal Process 2012;26:76–90.

[37] Zhu YC, Au SK. Bayesian operational modal analysis with asynchronous data, Part II: Posterior uncertainty. Mech Syst Signal Process 2018;98:920–35.

[38] Au SK. Connecting Bayesian and frequentist quantification of parameter uncertainty in system identification. Mech Syst Signal Process 2012;29:328–42.

[39] Au SK, Li B. Posterior uncertainty, asymptotic law and Cramér-Rao bound. Struct Control Heal Monit 2018;25:1–21.

[40] Au SK, Xie YL. Calculation of Hessian under constraints with applications to Bayesian system identification. Comput Methods Appl Mech Eng 2017;323:373–88.

[41] Petersen KB, Pedersen MS. The Matrix Cookbook (version: November 15, 2012). 2012.

[42] Au SK, Brownjohn JMW. Asymptotic identification uncertainty of close modes in Bayesian operational modal analysis. Mech Syst Signal Process 2019;133:106273.

[43] Au SK, Brownjohn JMW, Mottershead JE. Quantifying and managing uncertainty in operational modal analysis. Mech Syst Signal Process 2018;102:139–57.

[44] Au SK, Brownjohn JMW, Li B, Raby A. Understanding and managing identification uncertainty of close modes in operational modal analysis. Mech Syst Signal Process 2021;147:107018.

[45] Young J. Jiangyin Yangtze River Bridge, China. Proc. Inst. Civ. Eng. – Bridg. Eng., 2003, p. 45–53.

[46] Au SK. Fast Bayesian ambient modal identification in the frequency domain, Part I: Posterior most probable value. Mech Syst Signal Process 2012;26:60–75.

[47] Zhu Z. Bayesian Operational Modal Analysis with Multiple Setups and Multiple Modes. University of Liverpool, 2020.

[48] M. Brookes. The Matrix Reference Manual. [online] http://www.ee.imperial.ac.uk/hp/staff/dmb/matrix/intro.html; 2011.